Wind Turbulence over Misaligned Surface Waves and Air–Sea Momentum Flux. Part II: Waves in Oblique Wind

NYLA T. HUSAIN,[a] TETSU HARA,[a] AND PETER P. SULLIVAN[b]

[a] *Graduate School of Oceanography, University of Rhode Island, Narragansett, Rhode Island*
[b] *National Center for Atmospheric Research, Boulder, Colorado*

(Manuscript received 25 February 2021, in final form 8 November 2021)

ABSTRACT: The coupled dynamics of turbulent airflow and a spectrum of waves are known to modify air–sea momentum and scalar fluxes. Waves traveling at oblique angles to the wind are common in the open ocean, and their effects may be especially relevant when constraining fluxes in storm and tropical cyclone conditions. In this study, we employ large-eddy simulation for airflow over steep, strongly forced waves following and opposing oblique wind to elucidate its impacts on the wind speed magnitude and direction, drag coefficient, and wave growth/decay rate. We find that oblique wind maintains a signature of airflow separation while introducing a cross-wave component strongly modified by the waves. The directions of mean wind speed and mean wind shear vary significantly with height and are misaligned from the wind stress direction, particularly toward the surface. As the oblique angle increases, the wave form drag remains positive, but the wave impact on the equivalent surface roughness (drag coefficient) rapidly decreases and becomes negative at large angles. Our findings have significant implications for how the sea-state-dependent drag coefficient is parameterized in forecast models. Our results also suggest that wind speed and wind stress measurements performed on a wave-following platform can be strongly contaminated by the platform motion if the instrument is inside the wave boundary layer of dominant waves.

SIGNIFICANCE STATEMENT: Surface waves increase friction at the sea surface and modify how wind forces upper-ocean currents and turbulence. Therefore, it is important to include effects of different wave conditions in weather and climate forecasts. We aim to inform more accurate forecasts by investigating wind blowing over waves propagating in oblique directions using large-eddy simulation. We find that waves traveling at a 45° angle or larger to the wind grow as expected, but do not increase or even decrease the surface friction felt by the wind—a surprising result that has significant implications for how oblique wind-waves are represented as a source of surface friction in forecast models.

KEYWORDS: Wind stress; Wind waves; Air-sea interaction; Large eddy simulations

1. Introduction

Coupling between the ocean and atmosphere is driven by turbulent air–sea fluxes of momentum, energy, heat, and gases, and influences the evolution of marine weather and climate patterns. Constraining these air–sea fluxes in numerical models continues to be a challenge due to our incomplete understanding of near-surface air/water turbulence that is strongly modified by surface wave processes (Cronin et al. 2019).

Previous studies have addressed the impacts of surface waves on the wind profile and drag coefficient C_d (e.g., Moon et al. 2003, 2004, 2009; Fan et al. 2009; Donelan et al. 2012; Reichl et al. 2014), often focusing on key wave parameters such as the wave age and wave slope (e.g., Banner 1990; Belcher et al. 1993; Donelan et al. 1993; Makin and Kudryavtsev 1999; Donelan 2004; Donelan et al. 2006; Edson et al. 2013). In several modeling studies, sea-state-dependent C_d parameterizations based on full surface wave spectra have been developed to account for the effects of complex sea states in high to extreme winds, including conditions in which C_d saturates or even decreases with increasing wind speed (Moon et al. 2004; Hara and Belcher 2002, 2004; Fan et al. 2009; Donelan et al. 2012; Reichl et al. 2014). Constraining parameterizations of C_d, wave growth, and dissipation over a range of wave spectral conditions, including waves misaligned with and opposing wind, remains the focus of a very active area of research.

Several studies have aimed to address the effects of wind-wave misalignment (the difference between the wave direction and the wind speed direction θ) on wave growth and dissipation (e.g., Tolman and Chalikov 1996; Meirink et al. 2003; Kudryavtsev and Makin 2004; Ardhuin et al. 2007), as well as on the wind stress vector and C_d (Geernaert 1988; Geernaert et al. 1993; Bourassa et al. 1999; Grachev et al. 2003; Suzuki et al. 2010). Misalignment between wind and dominant surface waves occurs frequently in the open ocean over swells with low-to-moderate wind conditions (Donelan et al. 1997; Drennan et al. 1999; Donelan and Dobson 2001; Grachev et al. 2003; Ardhuin et al. 2007; Edson et al. 2007; Högström et al. 2015; Patton et al. 2019) as well as transient high wind conditions coupled to complex seas (Wright et al. 2001; Walsh et al. 2002; Black et al. 2007; Holthuijsen et al. 2012; Fan et al. 2009). Due to the challenges of in situ observations, the effects of wind-wave misalignment on the wind stress vector, drag coefficient, wave growth, and dissipation remain poorly

Corresponding author: Nyla Husain, nylahusain@uri.edu

DOI: 10.1175/JPO-D-21-0044.1

© 2022 American Meteorological Society. For information regarding reuse of this content and general copyright information, consult the AMS Copyright Policy (www.ametsoc.org/PUBSReuseLicenses).

Brought to you by University of Colorado Libraries | Unauthenticated | Downloaded 01/19/22 11:08 PM UTC

constrained. Even for typical wave fields with dominant waves aligned with the wind, real ocean wave spectra always contain significant contributions from misaligned waves. Therefore, improved understanding of the interaction between wind and misaligned waves is essential for developing models of sea-state-dependent drag coefficient.

In Part I of this study (Husain et al. 2021, hereafter Part I), we used LES to investigate the turbulent airflow over a steep wave train (ak = 0.27, k is wavenumber and a is wave amplitude) following and opposing wind for $|c/u_{*s}|$ = 1.4–11 (c is wave phase speed and u_{*s} is surface wind friction velocity). In particular, we have found a rather smooth transition in the near-surface airflow, from slow waves following wind to slow waves opposing wind to fast waves opposing wind, of increasingly stronger flow perturbations mainly caused by intermittent flow separations or separation-like patterns. The wave decay rate rapidly increases as the opposing wave speed increases, and our results are consistent with the recent LES study by Cao et al. (2020) and earlier observational and theoretical studies. We have also found that the effective roughness length (drag coefficient) rapidly increases as the opposing wave speed increases.

In Part II of this study, we use an identical LES approach of turbulent airflow over surface waves to expand on Part I by considering waves following and opposing wind at oblique angles (θ = 22.5°, 45°, 67.5°). Previous observational studies have proposed empirical scaling coefficients of the wave growth rate such as $\cos(\theta)$ (e.g., Plant 1982; Snyder et al. 1981) and $[U_{\lambda/2}\cos(\theta) - c]^2$ (e.g., Donelan 1999; Donelan et al. 2006, 2012). Previous theoretical studies tend to point toward $\cos^2(\theta)$ (e.g., Mastenbroek 1996; Burgers and Makin 1993; Li et al. 2000; Meirink et al. 2003). The latter two parameterizations are frequently used in existing wave prediction models. To our knowledge, the wave decay rate of waves opposing oblique wind has not been investigated. Furthermore, our understanding of the effects of obliquely propagating waves on the mean wind profile and drag coefficient remains limited.

The goal of this study (Part II) is to address how the wave growth/decay rate, mean wind profile (magnitude and direction), effective roughness length, and drag coefficient are modified by steep, strongly forced waves following/opposing oblique wind ($|c|/u_{*s} = 1.4$, ak = 0.27).

2. Methods

a. LES setup

We use an LES methodology of turbulent airflow over surface waves that is identical to previous studies (Sullivan et al. 2014; Hara and Sullivan 2015; Sullivan et al. 2018; Husain et al. 2019; Part I), all of which use pressure-driven channel flow over a wavy surface propagating through a domain with doubly periodic horizontal boundary conditions and a free-slip flat-top boundary. Here, we define time t, the along-wave x coordinate, the cross-wave y coordinate, and the vertical coordinate z pointing upward in the positive direction with z = 0 at the mean water surface. Velocities (u, υ, w) are in the (x, y, z) directions.

We consider a monochromatic wave train propagating in the x direction ($\partial/\partial y = 0$) with $h(x, t) = a\cos(kx - \omega t)$, where a is the wave amplitude, k is the wavenumber, ω is the angular frequency, and $c = \omega/k = \sqrt{g/k}$, identical to Part I. In LES, wind is driven by imposed horizontal pressure gradient $\nabla p = (\partial p/\partial x, \partial p/\partial y)$, which is balanced by the surface wind stress $|\tau_s| = u_{*s}^2 = |\nabla p| l_\zeta$, where l_ζ is the domain height. The total wind stress vector $\boldsymbol{\theta}$ is always pointed in the direction of $-\nabla p$, the angle of the external negative pressure gradient. Since we apply the free slip condition at the top boundary, the total wind stress linearly decreases from the wavy surface to the top.

For the actual LES, the waves always propagate in the positive x direction and the pressure gradient force (i.e., negative pressure gradient) is applied in the directions of 0°, 22.5°, 45°, 67.5°, 180°, 202.5°, 225°, and 247.5° (measured from the x axis in the counterclockwise direction; see Fig. 1, left panel). However, for the data analysis and discussion, the wave direction for the last two cases is reversed. Therefore, for the eight wind-wave conditions examined in this study, the wave directions are (0°, 0°, 0°, 0°, 180°, 180°, 180°, 180°) and the wind stress directions θ are (0°, 22.5°, 45°, 67.5°, 0°, 22.5°, 45°, 67.5°), respectively (see Fig. 1, right panel).

The subgrid and surface stress parameterizations are identical to those in Part I. The background surface roughness z_{ob} along the resolved wavy surface is set at a constant kz_{ob} = 2.7×10^{-3}, which accounts for the form drag of unresolved waves and the surface viscous stress. As in Part I we focus on a steep wave train of ak = 0.27. The wind forcing is set at $|c|/u_* = 1.4$ because we are mainly interested in strongly forced waves that support the bulk of the air–sea momentum flux (Donelan et al. 2012; Reichl et al. 2014).

Each simulation is run for approximately 100 000 time steps and averaged over the last 20 000 time steps after the wind field has reached a statistically steady state. Sullivan et al. (2014) and Sullivan et al. (2018) provide a full description of the LES algorithm and numerical methods used to solve the governing equations.

b. Data analysis

As in Part I we use a wave-following mapping and a coordinate system moving with the wave such that the wave shape is frozen and $h(x, t)$ becomes $h(\xi) = a\cos(k\xi)$. For more information on the wave-following mapping and the Jacobian transformation, refer to Hara and Sullivan (2015) and Part I. In particular, the contravariant vertical velocity perpendicular to the wave shape and constant ζ surfaces is defined as

$$W = \frac{1}{J} u \frac{\partial \zeta}{\partial x} + w, \tag{1}$$

where J is the Jacobian and is used to define uW and υW as vertical fluxes of x and y momentum across constant ζ surfaces due to the advective velocity W.

Using the triple decomposition (separating all relevant variables ψ into phase average $\bar{\psi}$ and turbulent ψ' components, and separating $\bar{\psi}$ into a horizontal mean $\langle\psi\rangle$ and wave coherent component $\tilde{\psi}$; see Hara and Sullivan 2015; Buckley and

Brought to you by University of Colorado Libraries | Unauthenticated | Downloaded 01/19/22 11:08 PM UTC

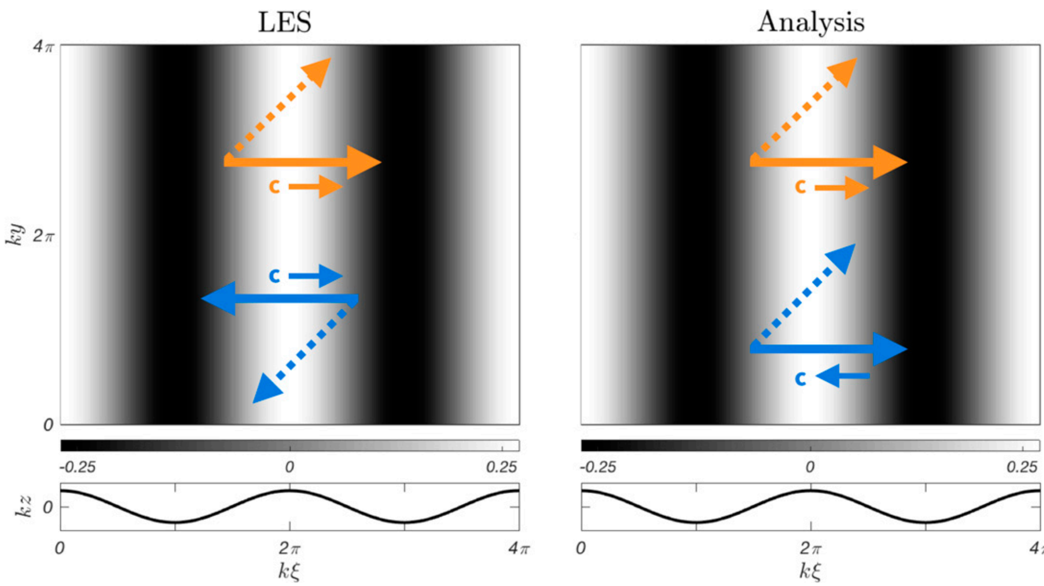

FIG. 1. Schematic of wind stress, wave phase speed, and surface wave elevation in the ξ–y coordinate for (left) the LES simulation and (right) data analysis. For simplicity, only the cases of θ = 0° (solid) and 45° (dashed) are shown. In LES, the direction of wave phase speed (c) is from left to right both for waves following wind (orange) and opposing wind (blue) with opposing wind stress directions determined by an external pressure gradient. In our data analysis, we present waves opposing wind (blue) with c directed from right to left and the wind stress in the same direction as waves following wind (orange).

Veron 2016; Husain et al. 2019; Part I), we can analyze the partition of the wind stress (momentum budget) in terms of turbulent and wave-coherent stresses as well as pressure stress in the along-wave direction. The addition of oblique wind adds a cross-wave (y) momentum budget to the along-wave (x) budget. The momentum budget is discussed in more detail in section 3d.

3. Results and discussion

In general, the flow field transitions smoothly as the wind stress direction θ increases from 0° to 22.5°, 45°, and 67.5°, i.e., as the wind-wave misalignment angle increases. Therefore, the discussions in this section mainly focus on comparing the flow field of oblique wind (θ = 45°) to that of aligned wind (θ = 0°). The results of θ = 22.5° and θ = 67.5° are included only when their impacts on the wave growth/decay rate and the equivalent roughness length (drag coefficient) are discussed.

a. 2D phase-averaged airflow

In this section, all flow fields presented are normalized by u_{*s} and k. In Figs. 2 (except the rightmost column), 3, 4, and 5, we display the two-dimensional phase-averaged flow fields (phase-average denoted by an overbar). In the top (bottom) two rows waves propagate from left to right (from right to left) in the positive (negative) x direction. In the first and third rows wind blows from left to right in the positive x direction. In the second and fourth rows the pressure gradient force and the resulting wind stress are in the direction rotated by 45° from the positive x direction. Consequently, the wind direction is also positively rotated from the x direction (by more than 45°, as discussed later). All the phase averaged flow fields are presented in the coordinate moving with the wave so that the flow fields are independent of t.

Figure 2 includes the streamwise velocity $[(\bar{u}-c)/u_{*s}]$, spanwise velocity $[(\bar{v})/u_{*s}]$, vertical velocity $(\bar{w}/u_{*s})$, and pressure $(\bar{p}/u_{*s}^2)$ plotted in rectangular (ξ–z) coordinates. In the rightmost column, the surface stress distribution is plotted for the total normal stress (pressure plus the turbulent normal stress), pressure only, and the along-wave turbulent tangential stress. Figure 3 includes the TKE magnitude $(\bar{e}/u_{*s}^2)$, the dissipation rate $[\epsilon/(ku_{*s}^3)]$, and the horizontal vorticity magnitude $\left[\overline{\omega_h}/(ku_{*s}) = \sqrt{\overline{\omega_x}^2+\overline{\omega_y}^2}/(ku_{*s})\right]$. Here, $\overline{\omega_x} = -(\partial\bar{v}/\partial z)+(\partial\bar{w}/\partial y)$ and $\overline{\omega_y} = (\partial\bar{u}/\partial z)-(\partial\bar{w}/\partial x)$ are dominated by the vertical shear of $\bar{v}$ and $\bar{u}$, respectively. Therefore, $\overline{\omega_h}$ is dominated by the vertical shear of oblique horizontal wind. Figure 4 shows the horizontal vorticity magnitude (same as Fig. 3) and the two components of the horizontal vorticity, $\overline{\omega_y}/(ku_{*s})$ and $-\overline{\omega_x}/(ku_{*s})$. Figure 5 includes the three components of the TKE. All quantities in Figs. 3–5 are plotted in the rectangular (ξ–z) coordinate as well as in the mapped (ξ–ζ) coordinate with the vertical axis in a log scale so that the flow fields very close to the wavy surface are magnified. Note that the results for waves following and opposing wind (first and third rows) are almost identical to the results presented in Part I for $c/u_{*s} = \pm 1.4$.

First, we examine the phase averaged velocity and pressure fields in Fig. 2. In the oblique wind cases with waves following or opposing wind, the along-wave velocity (in the

Brought to you by University of Colorado Libraries | Unauthenticated | Downloaded 01/19/22 11:08 PM UTC

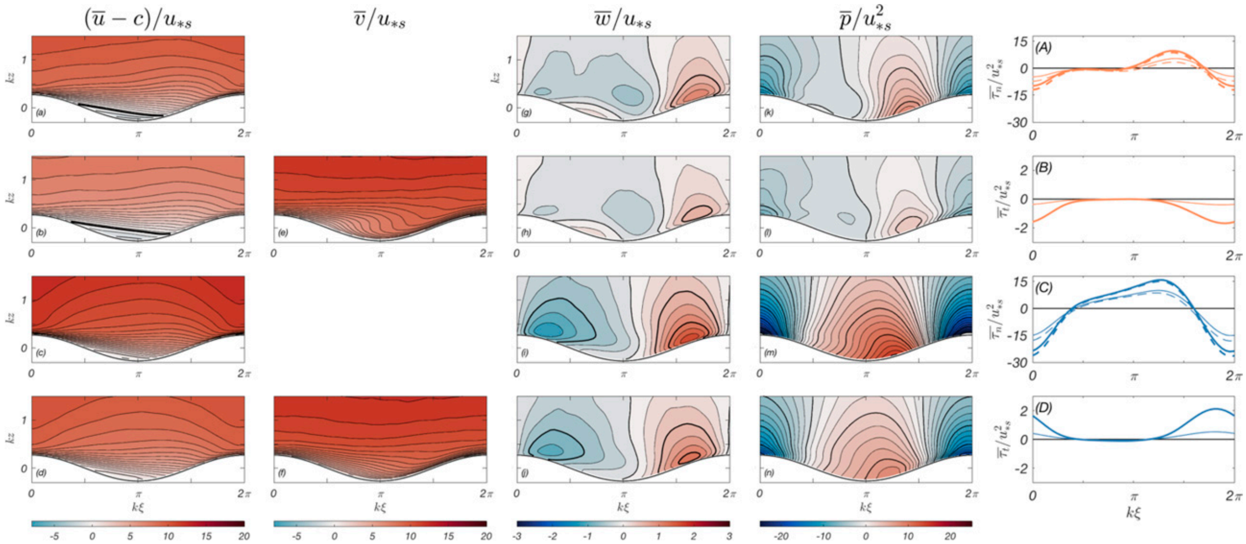

FIG. 2. Normalized phase-averaged flow fields in the ξ–z coordinate (top two rows) for waves following wind (oblique wind in second row) and (bottom two rows) for waves opposing wind (oblique wind in fourth row). From left to right: along-wave velocity [$(\overline{u} - c)/u_{*s}$], cross-wave velocity ($\overline{v}/u_{*s}$), vertical velocity ($\overline{w}/u_{*s}$), and pressure ($\overline{p}/u_{*s}^2$). Rightmost plots show the surface stress distribution for the normal stress $\overline{\tau_n}/u_{*s}^2$ (panels labeled A and C; solid line is total normal stress and dotted line is pressure only) and for the tangential stress $\overline{\tau_t}/u_{*s}^2$ in the x direction (panels labeled B and D) for waves (top two panels) following wind (orange lines) and (bottom two panels) opposing wind in aligned (thick lines) and oblique (thin lines) wind conditions.

x direction) is reduced, but the overall patterns remain very similar to those of the aligned wind cases (Figs. 2a–d). The cross-wave velocity (in the y direction) is introduced in the oblique cases (Figs. 2e,f) and is much stronger than the along-wave velocity (Figs. 2b,d). We will later show that even in a fixed coordinate, $\langle\overline{v}\rangle$ is larger than $\langle\overline{u}\rangle$, that is, the mean wind direction is rotated from the x direction by more than 45°. This is expected, at least qualitatively, because waves exert more friction (due to the wave form drag) and wind speed is more reduced in the along-wave (x) direction.

With the oblique wind, both the along-wave and cross-wave velocities are significantly reduced over the leeward face of the wave (Figs. 2b,d–f), suggesting that intermittent airflow separations (or separation-like flows) are modifying the wind fields, as in the aligned wind cases (Figs. 2a,c). The vertical velocity is slightly weaker in the oblique cases, but the patterns remain largely unchanged from the aligned cases (Figs. 2g–j).

As expected, the pressure along the wave phase weakens with oblique wind as less wind forcing is exerted onto the wave shape in the x direction (Figs. 2k–n), resulting in weaker

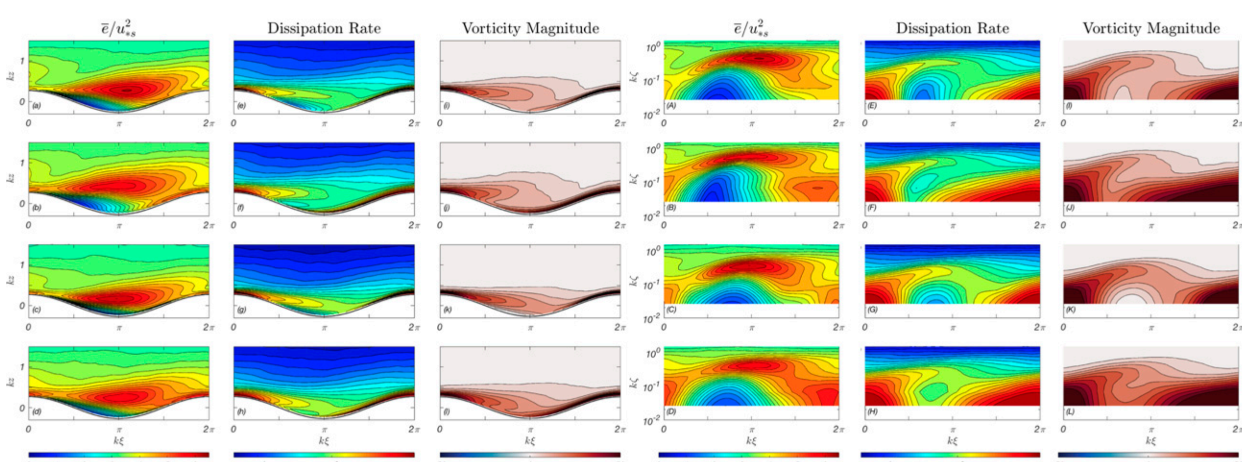

FIG. 3. (left three columns) Normalized phase-averaged flow fields in the ξ–z coordinate and (right three columns) the mapped ξ–ζ coordinate (top two rows) for waves following wind (oblique wind in second row) and (bottom two rows) for waves opposing wind (oblique wind in fourth row). From left to right: turbulent kinetic energy ($\overline{e}/u_{*s}^2$), dissipation rate $\left[\epsilon/\left(ku_{*s}^3\right)\right]$, and vorticity magnitude [$\overline{\omega}_h/(ku_{*s})$].

Brought to you by University of Colorado Libraries | Unauthenticated | Downloaded 01/19/22 11:08 PM UTC

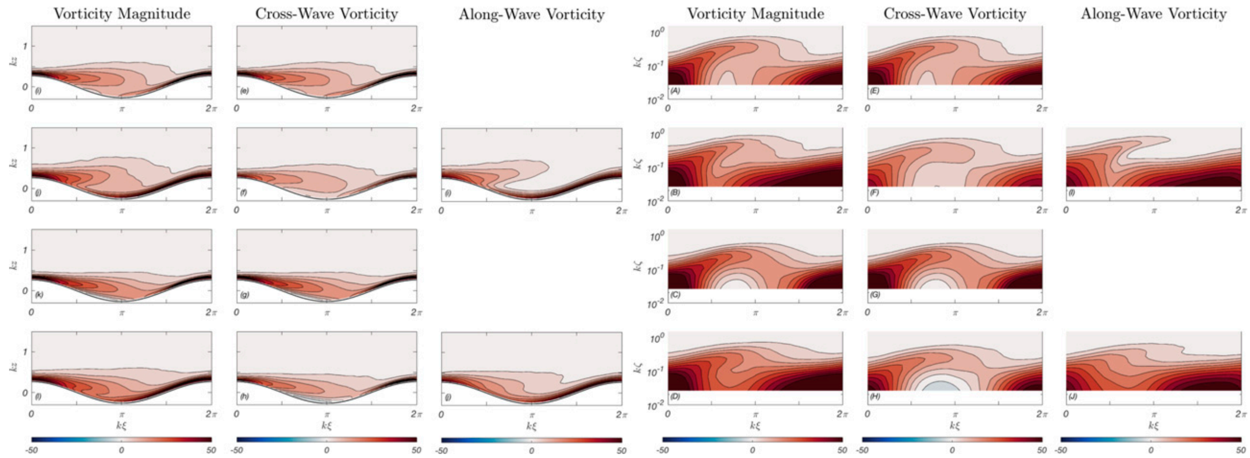

FIG. 4. (left three columns) Normalized phase-averaged flow fields in the ξ–z coordinate and (right three columns) the mapped ξ–ζ coordinate for (top two rows) waves following wind (oblique wind in second row) and (bottom two rows) waves opposing wind (oblique wind in fourth row). From left to right: vorticity magnitude $[\bar{\omega}_h/(ku_{*s})]$, cross-wave vorticity $[\bar{\omega}_y/(ku_{*s})]$, and along-wave vorticity $[-\bar{\omega}_x/(ku_{*s})]$.

surface pressure and total normal stress than in the aligned cases (Figs. 2A,C). Interestingly, the surface tangential stress in the along-wave direction is even more reduced with oblique winds (Figs. 2B,D), possibly because the horizontally averaged wind vector very close to the surface is rotated by almost 65°–68° from the x direction, as discussed later.

Next, we examine the phase averaged fields of TKE, dissipation rate, and horizontal vorticity magnitude in Fig. 3. For both aligned and oblique cases, regions of enhanced dissipation and vorticity appear to detach from the crest and extend downstream above the dead zone of significantly reduced TKE, dissipation rate, and vorticity on the leeward face of the wave. The enhanced TKE above the crest appears to be advected by the high velocity just above the detached high vorticity layer. These patterns are quite similar between the aligned and oblique wind cases, and suggest that flow is intermittently separating from the crest (or exhibiting separation-like patterns) even in oblique winds.

In general, the opposing and following wave cases in oblique winds are similar, except that the faster relative wind speed in the opposing case tends to limit the vertical extent of the wave induced flow perturbations closer toward the surface (cf. Figs. 3b,f,j,d,h,l). The same trend has been observed in the aligned wind cases in Part I.

One notable difference exists between the oblique and aligned wind cases. The high vorticity and high dissipation regions along the wavy surface are mostly confined near the crest in the aligned wind cases (Figs. 3E,G,I,K). However, these regions extend upstream all the way to the wave trough in the oblique wind cases (Figs. 3F,H,J,L). Consequently, the reduction of dissipation rate and vorticity in the dead zone is muted with the oblique wind.

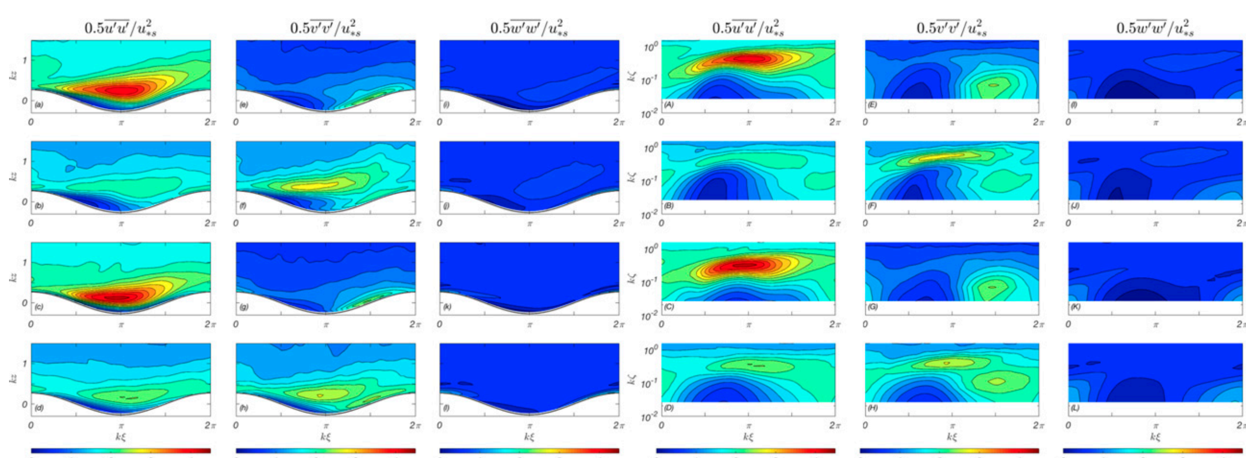

FIG. 5. (left three panels) Normalized phase-averaged flow fields in the ξ–z coordinate and (right three panels) the mapped ξ–ζ coordinate for (top two rows) waves following wind (oblique wind in second row) and (bottom two rows) waves opposing wind (oblique wind in fourth row). From left to right: the along-wave component $(0.5\overline{u'u'}/u_{*s}^2)$, the cross-wave component $(0.5\overline{v'v'}/u_{*s}^2)$, and the vertical component $(0.5\overline{w'w'}/u_{*s}^2)$ of TKE.

Brought to you by University of Colorado Libraries | Unauthenticated | Downloaded 01/19/22 11:08 PM UTC

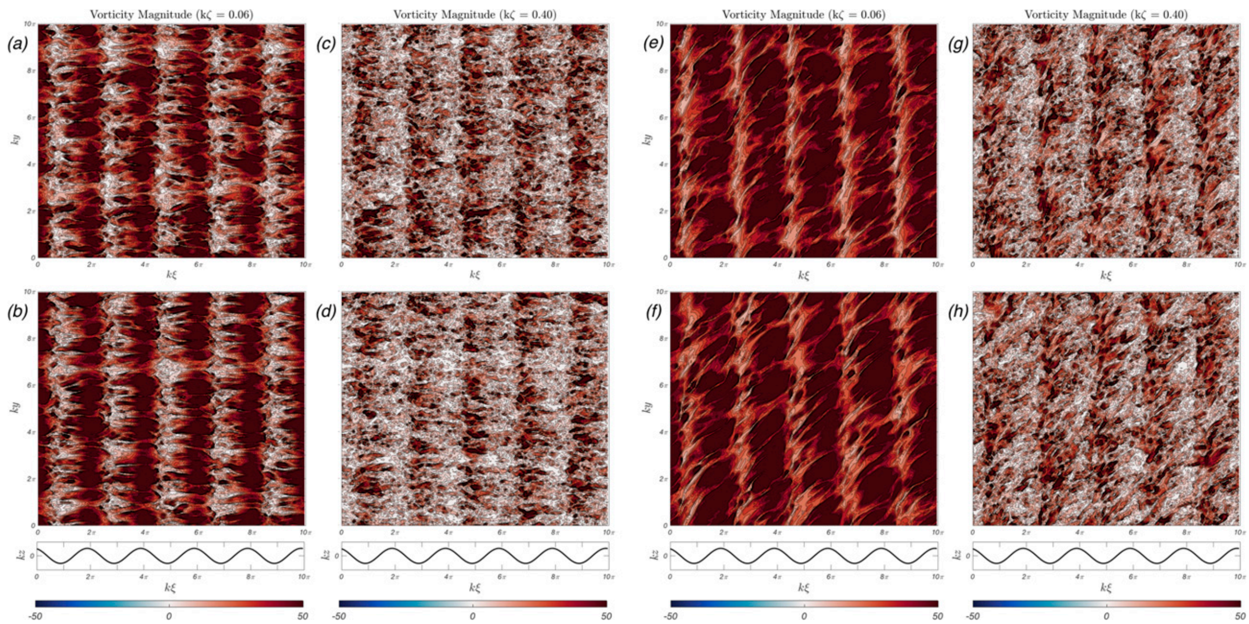

FIG. 6. Normalized instantaneous vorticity magnitude $[\omega_h/(ku_{*s})]$ fields in the ξ–y coordinate (top) for waves following wind and (bottom) for waves opposing wind in (a)–(d) aligned wind and (e)–(h) oblique wind at heights of $k\zeta = 0.06$ in (a), (b), (e), and (f) and $k\zeta = 0.40$ in (c), (d), (g), and (h).

To shed more light on these features, we next examine the along-wave and cross-wave vorticity components separately in Fig. 4. It is clear that the detached layer of enhanced vorticity is present in both directions (Figs. 4F,I,H,J) in the oblique cases. The crosswind vorticity simply weakens in oblique winds, but its patterns remain very similar between the aligned and oblique cases with reduced vorticity in the dead zone (Figs. 4E–H). In contrast, the along-wave vorticity remains strong along the entire surface, and especially along the windward face and the crest of the wave (Figs. 4I,J). This enhanced along-wind vorticity appears to be well correlated with the enhanced dissipation in the same location (Figs. 3F,H). The enhancement of along-wind vorticity and dissipation rate on the windward side of the crest (between the trough and following crest) may be related to reattachment of the separated oblique wind flow. We will later show that the cross-wave wave-coherent velocity $\tilde{v}$ is also enhanced there.

One interesting feature for waves opposing oblique winds is the presence of a region of negative cross-wave vorticity near the trough (Fig. 4H). In Part I, we have shown that for waves opposing wind a region of negative cross-wave vorticity near the trough intensifies as waves get faster, and is associated with separation-like detachment of airflow from the surface. In such a region wind shear is negative; that is, the wind speed decreases with height. However, in the case of oblique wind, the mean wind direction is close to 70° (as explained later) and the along-wave vorticity remains strong in the same region. Therefore, the wind speed magnitude increases with height.

In Fig. 5, we separate the TKE into along-wave $(0.5\overline{u'u'}/u_{*s}^2)$, cross-wave $(0.5\overline{v'v'}/u_{*s}^2)$, and vertical $(0.5\overline{w'w'}/u_{*s}^2)$ components. As expected, in aligned winds the TKE is dominated by the along-wave component (Figs. 5a,c,A,C). One notable exception is a region on the windward side of the crest near the surface, where the cross-wave component is significantly enhanced and is larger than the along-wave component (Figs. 5e,g,E,G). The cause of this enhancement is not clear, but it may be related to the reattachment of separated flow in this area.

In the oblique case, the along-wave component of the TKE is drastically reduced and the cross-wave component is significantly larger. This is consistent with the fact that both mean wind speed and mean wind shear are rotated by more than 45° from the x axis, as discussed later. The enhancement of the cross-wave component on the windward side of the crest is observed in the oblique wind cases as well (Figs. 5f,h,F,H). This enhancement is possibly related to the enhanced along-wind vorticity (Figs. 4I,J) with large $\partial\overline{v}/\partial z$ in the same area. Finally, the consistently small vertical component suggests that the airflow turbulence is dominated by horizontal velocity variances in the entire wave boundary layer.

b. *Instantaneous vorticity fields*

To demonstrate the transient character of the flow field over waves in oblique wind, in Fig. 6 we display instantaneous snapshots of horizontal vorticity magnitude $[\omega_h/(ku_{*s})]$ from a mapped top-down view (in the ξ–y coordinate) at $k\zeta = 0.06$ (very close to the surface) and at $k\zeta = 0.40$ for waves aligned with wind (left four plots) and waves oblique to wind (right four plots). For these snapshots, we are using the resolved fields and appreciate that very near the surface the total vorticity fluctuations are underestimated. Very close to the surface, the waves strongly modify the horizontal vorticity magnitude. In aligned wind, a pattern of enhanced vorticity is

Brought to you by University of Colorado Libraries | Unauthenticated | Downloaded 01/19/22 11:08 PM UTC

present near the surface along the crest with a sudden reduction downwind where airflow intermittently separates (Figs. 6a,b). The wave signature diminishes with height (Figs. 6c,d), but the enhanced vorticity is now observed further downstream from the crest, suggesting the advected high vorticity due to flow separations and being consistent with Figs. 4A and 4C.

In oblique wind near the surface ($k\zeta = 0.06$), the areas of enhanced vorticity magnitude are significantly expanded from the crest toward the upwind trough compared with the aligned wind cases, as expected from Figs. 4B and 4D. The region of reduced vorticity just downstream of the crest is narrower. Their pattern is also modified since it is aligned with the oblique mean wind direction. Similar to the aligned case, the signature of advected high vorticity is still visible at $k\zeta = 0.40$.

c. Horizontally averaged wind profiles in mapped coordinates

Next, we investigate the vertical profiles of the horizontally averaged wind variables in the mapped (ζ) coordinate, including mean wind speed, mean wind shear, TKE and its components, shown in Fig. 7. In the following subsections profiles for waves following (opposing) aligned wind are shown as thick orange (blue) lines, and profiles for waves following (opposing) oblique wind are shown as thin orange (blue) lines. All the profiles are displayed up to $k\zeta = 2$.

The four panels in the top row of Fig. 7 display vertical profiles of the horizontally averaged mean wind speed vector. The x and y components of the wind vector, $\langle u\rangle/u_{*s}$ and $\langle v\rangle/u_{*s}$, are shown in Figs. 7a and 7d, respectively, while their magnitude, $\left(\langle u\rangle^2+\langle v\rangle^2\right)^{1/2}/u_{*s}$, and angle, $\theta = \arctan(\langle v\rangle/\langle u\rangle)$, are shown in Figs. 7g and 7j, respectively. The gray lines in Figs. 7a and 7d represent the flat wall wind speed profiles with a background roughness of $kz_{ob} = 2.70 \times 10^{-3}$, for aligned (thick lines) and oblique (thin lines) cases, for linearly decreasing wind stress (solid) and constant wind stress (dashed) in $k\zeta$. In Fig. 7g the thick gray lines apply for both aligned and oblique cases. The thin dashed gray line in Fig. 7j represents the angle of the flat wall wind speed profile, $\theta = 45°$, which is equal to the angle of the wind stress and the imposed pressure gradient.

As discussed in Part I, the wind speed magnitude (Fig. 7g) in the aligned cases (thick orange and blue lines) is significantly reduced from the wind profile for a flat wall (thick gray line) near the top of the domain, indicating that the equivalent surface roughness is increased for both waves following and opposing wind, with the latter having a slightly higher roughness length. However, the wind speed magnitude in the oblique cases (thin orange and blue lines) is very close to that for a flat wall (thick gray line) near the top of the domain for both waves following and opposing the oblique wind, which indicates that the waves do not enhance the equivalent surface roughness above the background roughness (more discussions follow in section 3f).

If we examine the along-wave and cross-wave wind speeds separately (Figs. 7a,d) for the oblique cases, it is clear that both components are significantly modified by the wave. As expected, the along-wave wind speed is reduced from the flat wall profile because of the wave form drag. The along-wave wind profiles for oblique wind are roughly proportional to those for aligned wind, and are reduced by about 25%–30% throughout the wave boundary layer. Interestingly, the cross-wave wind speed is increased near the top of the domain compared to the flat wall wind speed (Fig. 7d). The combined effect of increased cross-wave wind speed and decreased along-wave wind speed yields the almost unchanged wind speed magnitude toward the top.

The opposite wave impacts on the along-wave and cross-wave wind speeds mean that the angle of the wind speed (θ = 52°–54°) is significantly misaligned from the angle of the wind stress ($\theta = 45°$) near the top of the domain (Fig. 7j), even though the wind magnitude is not modified by the wave. The wind speed angle is much larger closer to the surface, falling between $\theta = 65°$ and 68°. From about $k\zeta$ = 0.1–0.4, the angle quickly reduces to about $\theta \approx 55°$, and reduces more slowly from there to the top at $k\zeta = 2$. It is notable that the wind speed angle is strongly dependent on height in the wave boundary layer, and that its misalignment from the total wind stress angle ($\theta = 45°$) appears to persist above the top of the wave boundary layer.

The second row of Fig. 7 displays vertical profiles of the normalized mean wind shear. Figures 7b and 7e show the along-wave and cross-wave shear, $(\partial\langle u\rangle/\partial\zeta)(\kappa\zeta/u_{*s})$ and $(\partial\langle v\rangle/\partial\zeta)(\kappa\zeta/u_{*s})$, respectively, and Figs. 7h and 7k show the wind shear magnitude and the wind shear angle (solid lines), respectively. The gray lines represent the flat wall wind shear profiles as in the first row.

The shape of vertical profiles of wind shear magnitude (Figs. 7h) is quite similar between the aligned and oblique wind cases, with a reduction near the surface and enhancement at midlevel. However, the wind shear magnitude for the oblique wind is consistently larger throughout the wave boundary layer (compare thin orange line with thick orange line, or thin blue line with thick blue line). This larger wind shear magnitude is responsible for the larger wind speed near the top of the domain (Fig. 7g) and the resulting smaller equivalent roughness length.

The along-wave wind shear profiles (Fig. 7b) for the oblique wind cases are roughly proportional to those for the aligned wind cases (except near the top where they collapse); they are reduced by about 25%–30%. This suggests that the same physical processes (i.e., effects of pressure form drag near the surface and of intermittent airflow separations at midlevel) take place in oblique wind cases, but their impacts are reduced. Near the top of the wave boundary layer, the along-wave wind shear is not much reduced for the oblique cases, and this contributes to the enhanced wind shear magnitude near the top.

In the middle of the wave boundary layer, the cross-wave wind shear profiles (Fig. 7e) for the oblique wind cases are significantly enhanced compared to that for a flat wall case, and this contributes to the enhancement of the wind shear magnitude and far field wind speed as well as the reduced equivalent roughness length. The shear enhancement occurs at lower elevation with waves opposing (compared to following) oblique wind, which is consistent with the earlier observation

Brought to you by University of Colorado Libraries | Unauthenticated | Downloaded 01/19/22 11:08 PM UTC

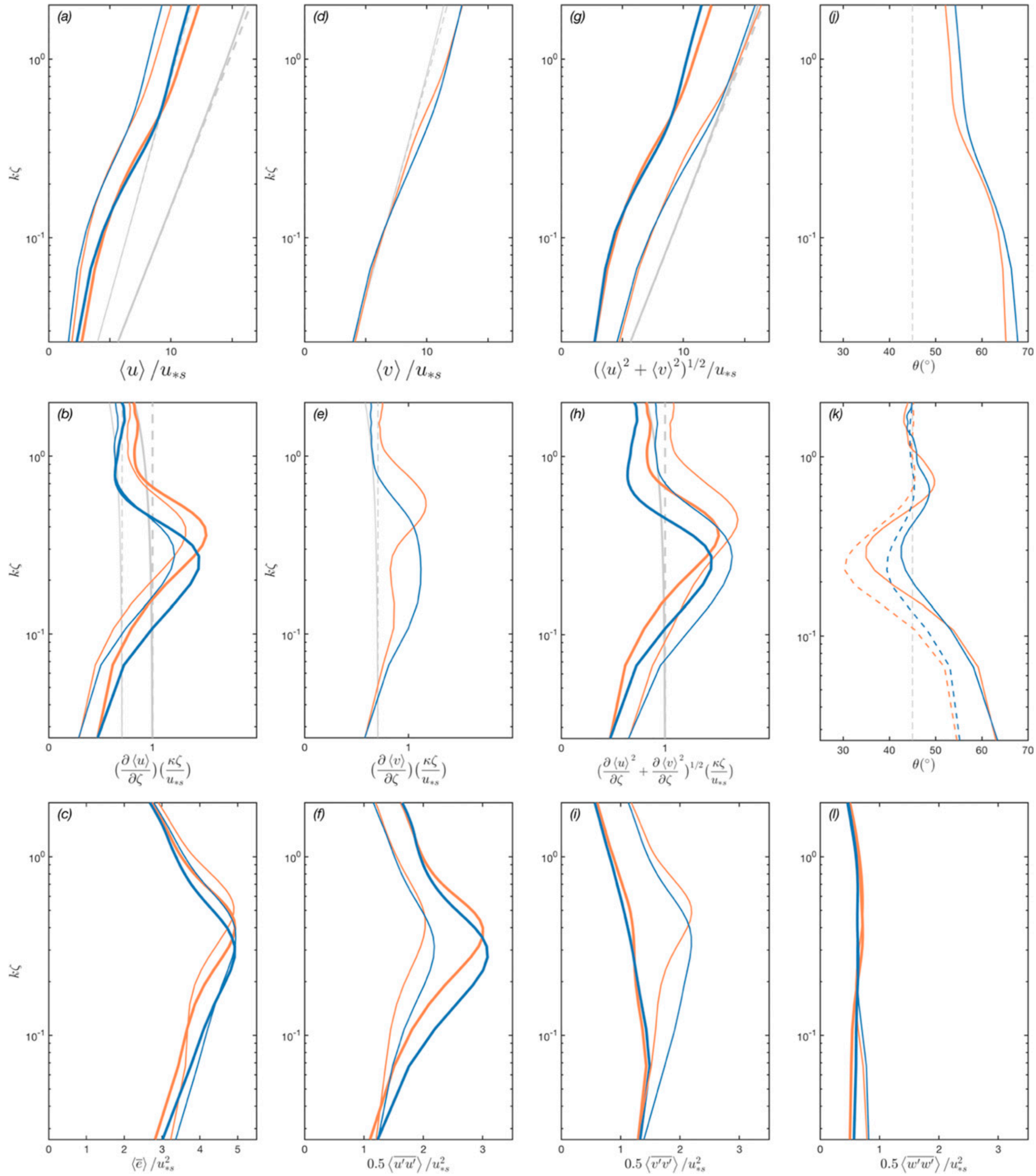

FIG. 7. (a),(d),(g),(j) Normalized vertical profiles of horizontally averaged along-wave wind speed ($\langle u \rangle / u_{*s}$), cross-wave wind speed ($\langle v \rangle / u_{*s}$), wind speed magnitude, and wind speed angle. (b),(e),(h),(k) Normalized vertical profiles of horizontally averaged along-wave wind shear [$(\partial \langle u \rangle / \partial \zeta)(\kappa \zeta / u_{*s})$], cross-wave wind shear [$(\partial \langle v \rangle / \partial \zeta)(\kappa \zeta / u_{*s})$], wind shear magnitude, and wind shear angle. In (k) dashed lines show angle of horizontally averaged turbulent stress vector ($\langle \tau_{13}^t \rangle$, $\langle \tau_{23}^t \rangle$). (c),(f),(i),(l) Normalized vertical profiles of horizontally averaged TKE magnitude ($\langle \bar{e} \rangle / u_{*s}^2$), the along-wave component ($0.5\langle \overline{u'u'} \rangle / u_{*s}^2$), the cross-wave component ($0.5\langle \overline{v'v'} \rangle / u_{*s}^2$), and the vertical component ($0.5\langle \overline{w'w'} \rangle / u_{*s}^2$) of the TKE. In all panels, profiles for waves following (opposing) aligned wind are shown as thick orange (blue) lines, and profiles for waves following (opposing) oblique wind are shown as thin orange (blue) lines. Gray lines show profiles for flat wall cases (explained in the main text).

Brought to you by University of Colorado Libraries | Unauthenticated | Downloaded 01/19/22 11:08 PM UTC

that waves opposing wind tend to suppress the vertical extent of the wave induced flow perturbations.

The angle of the mean wind shear is plotted in Fig. 7k (solid lines), along with the angle of the horizontally averaged turbulent stress (dashed lines; more discussion on the turbulent stress and momentum budget in the next subsection). Both the wind shear angle and the turbulent stress angle hover around $\theta = 45°$ above $k\zeta = 1$; that is, the mean wind shear and the turbulent stress are well aligned with the total wind stress there. This suggests that the direction of the mean wind speed gradually approaches the wind stress direction (i.e., the misalignment between wind speed and wind stress gradually disappears) if the constant stress layer is extended upward without a top boundary (i.e., in the open ocean condition).

At midlevel, the wind shear angle oscillates around 45° for waves opposing wind, but it is significantly reduced from 45° at around $k\zeta = 0.30$ for waves following wind, associated with the enhancement of the along-wave wind shear (Fig. 7b). Toward the surface, the wind shear angle increases to about $\theta = 63°$.

The profiles of the wind shear angle (solid lines) are generally well correlated with the profiles of the turbulent stress angle (dashed lines). This observation supports the common turbulence closure assumption that the angle of the turbulent wind stress is the same as the angle of the mean wind shear (i.e., the momentum flux is downgradient). However, toward the surface the angle of the turbulent stress is consistently smaller than the angle of the mean wind shear by about 8°–9°.

The bottom row of Fig. 7 displays vertical profiles of the horizontally averaged TKE and its three components. With the oblique wind, the magnitude of TKE remains largely unchanged (Fig. 7c). However, the profiles of along-wave TKE and cross-wave TKE significantly differ between the oblique and aligned cases. In aligned winds, the along-wave TKE component is much larger and is pronounced at midlevel, associated with flow separation (or separation-like) patterns (see also Figs. 4A,C). In oblique winds, the cross-wave TKE component is larger, and both components show modest enhancement at midlevel (see also Figs. 4B,D,F,H). The vertical TKE component remains significantly smaller throughout the wave boundary layer.

d. *Horizontally averaged momentum budget in along-wave and cross-wave directions*

As discussed in section 2b, the momentum budget must be satisfied in both along-wave (x) and cross-wave (y) directions. Specifically, the normalized x and y momentum equations may be expressed as

$$\frac{\langle\tau_{13}^{w}\rangle + \langle\tau_{13}^{p}\rangle}{\tau_s} + \frac{\langle\tau_{13}^{t}\rangle}{\tau_s} + \frac{\frac{\partial P}{\partial x}\,\zeta}{\tau_s} = \cos(\theta) \tag{2a}$$

$$\frac{\langle\tau_{23}^{w}\rangle}{\tau_s} + \frac{\langle\tau_{23}^{t}\rangle}{\tau_s} + \frac{\frac{\partial P}{\partial y}\,\zeta}{\tau_s} = \sin(\theta) \tag{2b}$$

where θ is the direction of the total wind stress (applied negative pressure gradient), $\langle\tau_{13}^{w}\rangle = \langle\tilde{u}\tilde{W}\rangle$ and $\langle\tau_{23}^{w}\rangle = \langle\tilde{v}\tilde{W}\rangle$ are the along-wave and cross-wave components of the wave-coherent stress, and $\langle\tau_{13}^{t}\rangle = \langle u'W'\rangle$ and $\langle\tau_{23}^{t}\rangle = \langle v'W'\rangle$ are the along-wave and cross-wave components of the turbulent stress (including both the resolved and parameterized subgrid-scale stress). The pressure (form) stress is defined as $\tau_{13}^{p} = (1/J)\bar{p}(\partial\zeta/\partial x)$ (see Hara and Sullivan 2015; Part I) and is only present in the x momentum equation because the wave shape does not change in the cross-wave direction.

The horizontally averaged momentum budget (or wind stress partition) for the along-wave and cross-wave directions as described in Eq. (2) is shown in Fig. 8. Similar to Fig. 7, the solid (dashed) gray lines represent the values for the flat wall case with linearly decreasing (constant) total wind stress in $k\zeta$. The total stress $(\langle\tau_{13}^{\mathrm{tot}}\rangle, \langle\tau_{23}^{\mathrm{tot}}\rangle)$, which has been calculated by adding the wave-coherent stress $(\langle\tau_{13}^{w}\rangle, \langle\tau_{23}^{w}\rangle)$, turbulent stress $(\langle\tau_{13}^{t}\rangle, \langle\tau_{23}^{t}\rangle)$, and pressure stress $(\langle\tau_{13}^{p}\rangle, 0)$, is almost identical to the gray solid lines, indicating that the momentum budget is well satisfied in both directions.

In Figs. 8a and 8c the vertical profiles of all stress components in the along-wave direction are similar between the aligned and oblique cases; the values in the oblique case are simply reduced roughly in proportion to the reduction of total stress. In both cases, the pressure stress magnitude increases toward the surface, and the wave-coherent stress is positively (upward momentum flux) enhanced at midlevel ($k\zeta \approx$ 0.3–0.5). The turbulent stress magnitude is reduced near the surface to compensate the pressure stress, and is enhanced at midlevel to compensate the wave-coherent stress.

In Figs. 8b and 8d, the pressure stress is zero in the cross-wave direction with no wave shape, but the turbulent and wave-coherent stresses are strongly modulated by the wave. In particular, for waves following oblique wind the negative wave-coherent stress $\langle\tau_{23}^{w}\rangle$ (downward momentum flux) is significantly enhanced around $k\zeta$ = 0.2–0.3, and the turbulent stress $\langle\tau_{23}^{t}\rangle$ is reduced to compensate it. This reduction of $\langle\tau_{23}^{t}\rangle$ is reflected in the decrease of the turbulent stress direction at the same level (Fig. 7k), which is well correlated with the reduced mean wind shear direction.

In summary, the cross-wave component of the wave-coherent stress is totally different from its along-wave component, and thus modifies the cross-wave turbulent stress in a distinct way. Therefore, the wave-coherent stress seems to play an important role in modifying the magnitude and direction of turbulent stress and mean wind shear, and modifying the mean wind profile in a complex manner.

To better understand the wave modulated turbulent and wave-coherent stresses, we examine the phase-averaged 2D fields of turbulent stress, wave-coherent stress, and wave-coherent velocities, $\tilde{u}$, $\tilde{v}$, $\tilde{W}$, in Fig. 9. In the along-wave direction, the 2D pattern of wave-coherent stress $\overline{\tau_{13}^{w}} = \tilde{u}\tilde{W}$ is very similar in all cases (Figs. 9g–j). Strong upward momentum flux (positive $\tilde{u}\tilde{W}$) occurs in two areas due to flow separation and reattachment. Namely, just downstream of the crest the accelerated fluid (positive $\tilde{u}$) is carried away from the surface (positive $\tilde{W}$), and just downstream of the trough the decelerated fluid (negative $\tilde{u}$) returns toward the surface (negative $\tilde{W}$) (Figs. 9m–t). The combined effect introduces large upward momentum flux if averaged horizontally (Fig. 8c). In oblique wind, the along-wave wave-coherent velocities and

Brought to you by University of Colorado Libraries | Unauthenticated | Downloaded 01/19/22 11:08 PM UTC

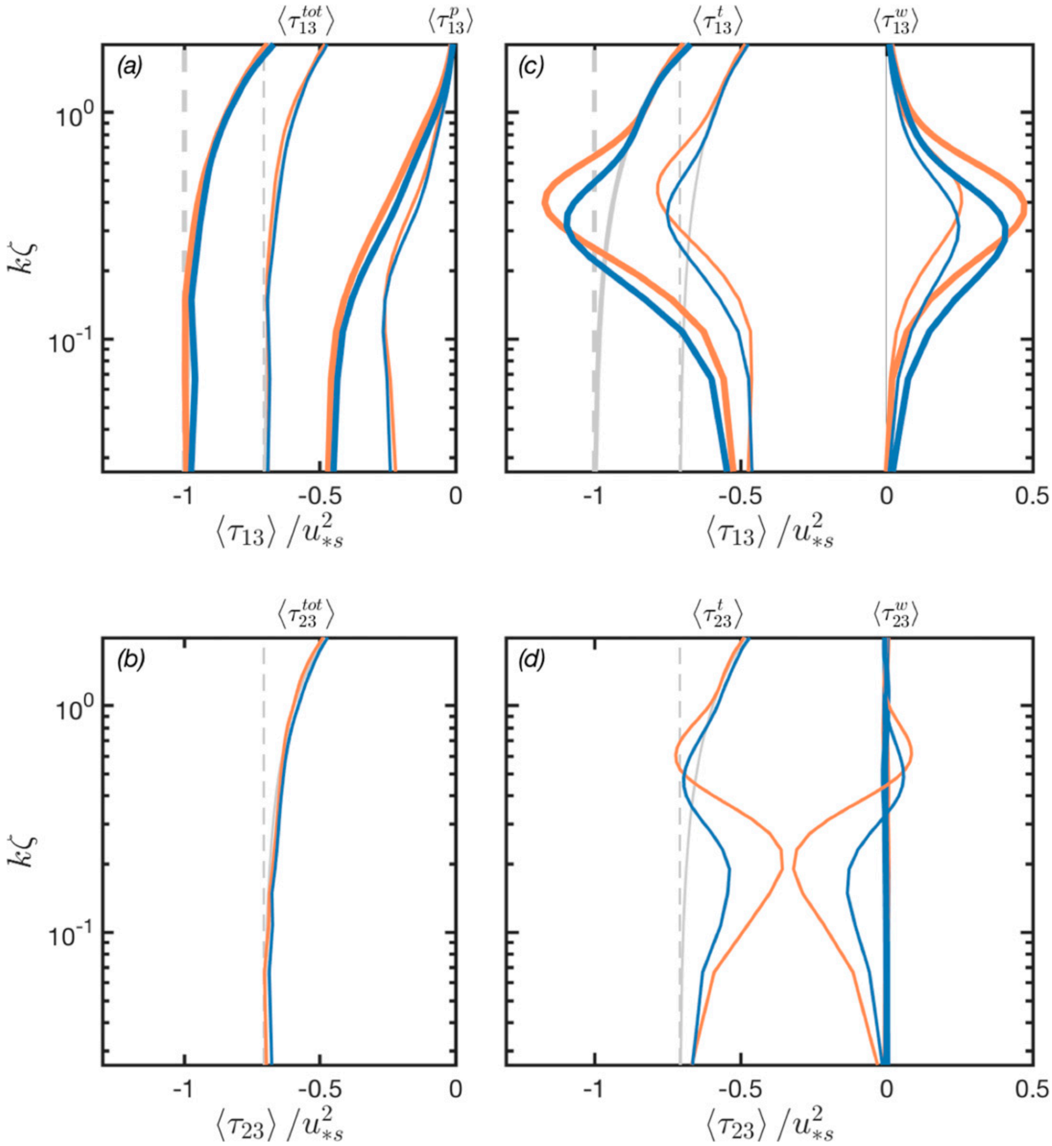

FIG. 8. Normalized vertical profiles of horizontally averaged momentum budget terms following wind (orange lines) and opposing wind (blue lines) for oblique (thin lines) and aligned (thick lines) wind conditions. In the top row, the along-wave (x) momentum budget includes total wind stress in the x direction ($\langle\tau_{13}^{\mathrm{tot}}\rangle/u_{*s}^2$), pressure stress ($\langle\tau_{13}^{p}\rangle/u_{*s}^2$), along-wave turbulent stress ($\langle\tau_{13}^{t}\rangle/u_{*s}^2$), and along-wave wave-coherent stress ($\langle\tau_{13}^{w}\rangle/u_{*s}^2$). In the bottom row, the cross-wave (y) momentum budget includes total wind stress in the y direction ($\langle\tau_{23}^{\mathrm{tot}}\rangle/u_{*s}^2$), cross-wave turbulent stress ($\langle\tau_{23}^{t}\rangle/u_{*s}^2$), and cross-wave wave-coherent stress ($\langle\tau_{23}^{w}\rangle/u_{*s}^2$). Gray lines show profiles for flat wall cases (explained in the main text).

stresses are weakened, but their patterns remain qualitatively similar. To compensate the upward wave-coherent stress, the negative turbulent stress $\overline{\tau_{13}^{t}}$ is significantly enhanced above the windward side of the crest (dark blue regions in Figs. 9a–d).

A pair of similar but much weaker areas of positive wave-coherent stress ($\overline{\tau_{23}^{w}} = \tilde{v}\tilde{W}$) are observed in the cross-wave direction as well (red areas in Figs. 9k,l). However, they are dwarfed by a pair of much stronger downward momentum flux (negative $\tilde{v}\tilde{W}$) regions (blue areas in Figs. 9k,l). This downward flux is caused by the large perturbation of $\tilde{v}$ along the wave phase. Namely, $\tilde{v}$ is negative between the leeward crest and the leeward trough, and is positive between the windward trough and the following crest. The separating flow (positive $\tilde{W}$) carries the fluid with negative $\tilde{v}$ away from the surface, and reattaching flow (negative $\tilde{W}$) brings the fluid with positive $\tilde{v}$ back toward the surface (Figs. 9m–p,u,v). The resulting downward flux is particularly strong for waves

Brought to you by University of Colorado Libraries | Unauthenticated | Downloaded 01/19/22 11:08 PM UTC

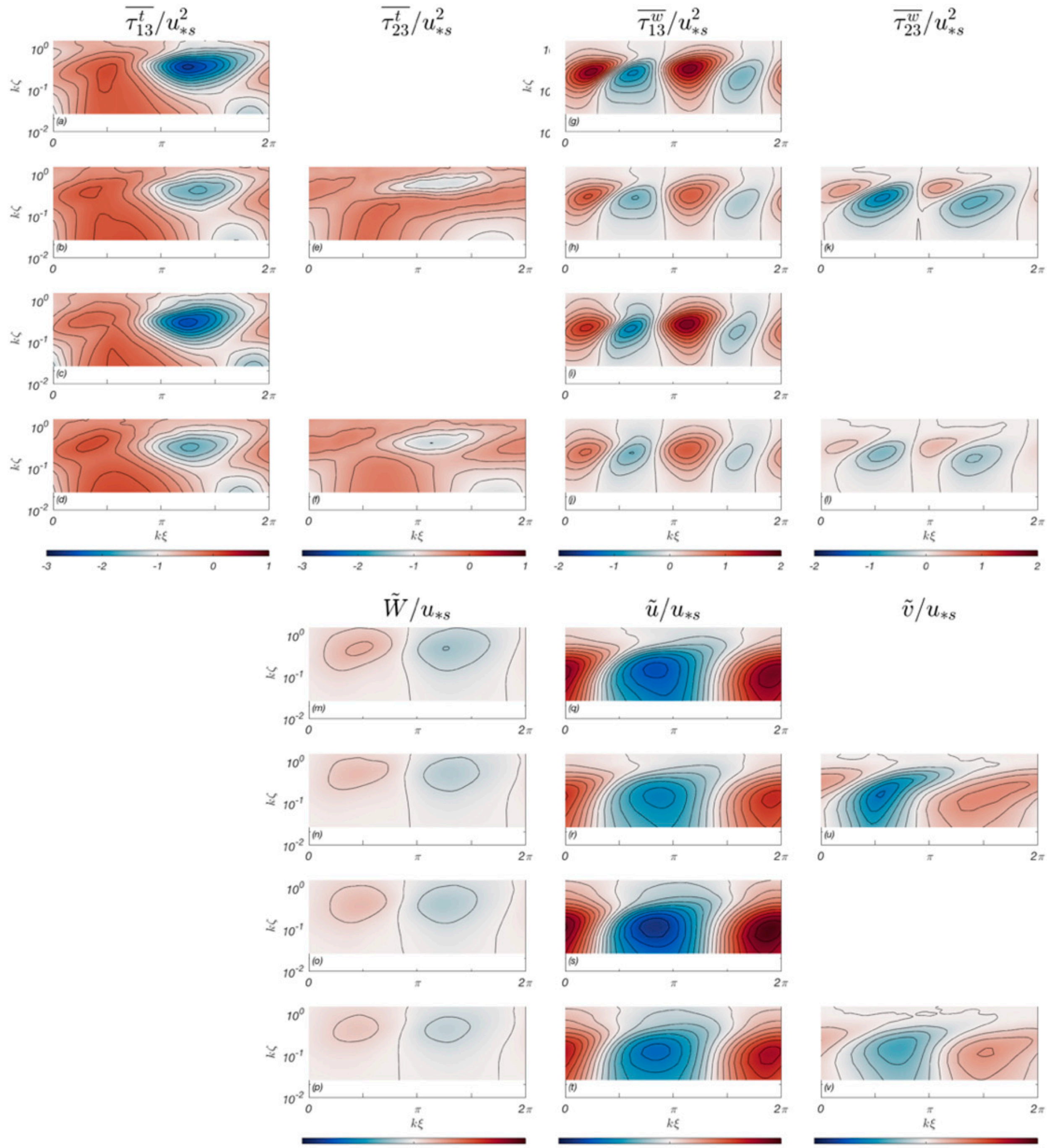

FIG. 9. Top four rows show normalized phase-averaged fields of the along-wave turbulent stress ($\overline{\tau^t_{13}}/u^2_{*s} = \overline{u'W'}/u^2_{*s}$), cross-wave turbulent stress ($\overline{\tau^t_{23}}/u^2_{*s} = \overline{v'W'}/u^2_{*s}$), along-wave wave-coherent stress ($\overline{\tau^w_{13}}/u^2_{*s} = \tilde{u}\tilde{W}/u^2_{*s}$), and cross-wave wave-coherent stress ($\overline{\tau^w_{23}}/u^2_{*s} = \tilde{v}\tilde{W}/u^2_{*s}$) in the mapped ξ–ζ coordinate. From top to bottom: waves following aligned wind, waves following oblique wind, wave opposing aligned wind, and waves opposing oblique wind. Bottom four rows show normalized phase-averaged fields of the wave-coherent vertical velocity ($\tilde{W}/u_{*s}$), along-wave velocity ($\tilde{u}/u_{*s}$), and cross-wave velocity ($\tilde{v}/u_{*s}$)in the mapped ξ–ζ coordinate.

following oblique wind. This enhanced downward wave-coherent stress is compensated by the reduced downward turbulent stress (Figs. 9e,f).

The strong wave-coherent velocities $\tilde{u}$ and $\tilde{v}$ suggest that the phase averaged flow magnitude and direction are strongly phase dependent. In Fig. 10, a top-down view is

Brought to you by University of Colorado Libraries | Unauthenticated | Downloaded 01/19/22 11:08 PM UTC

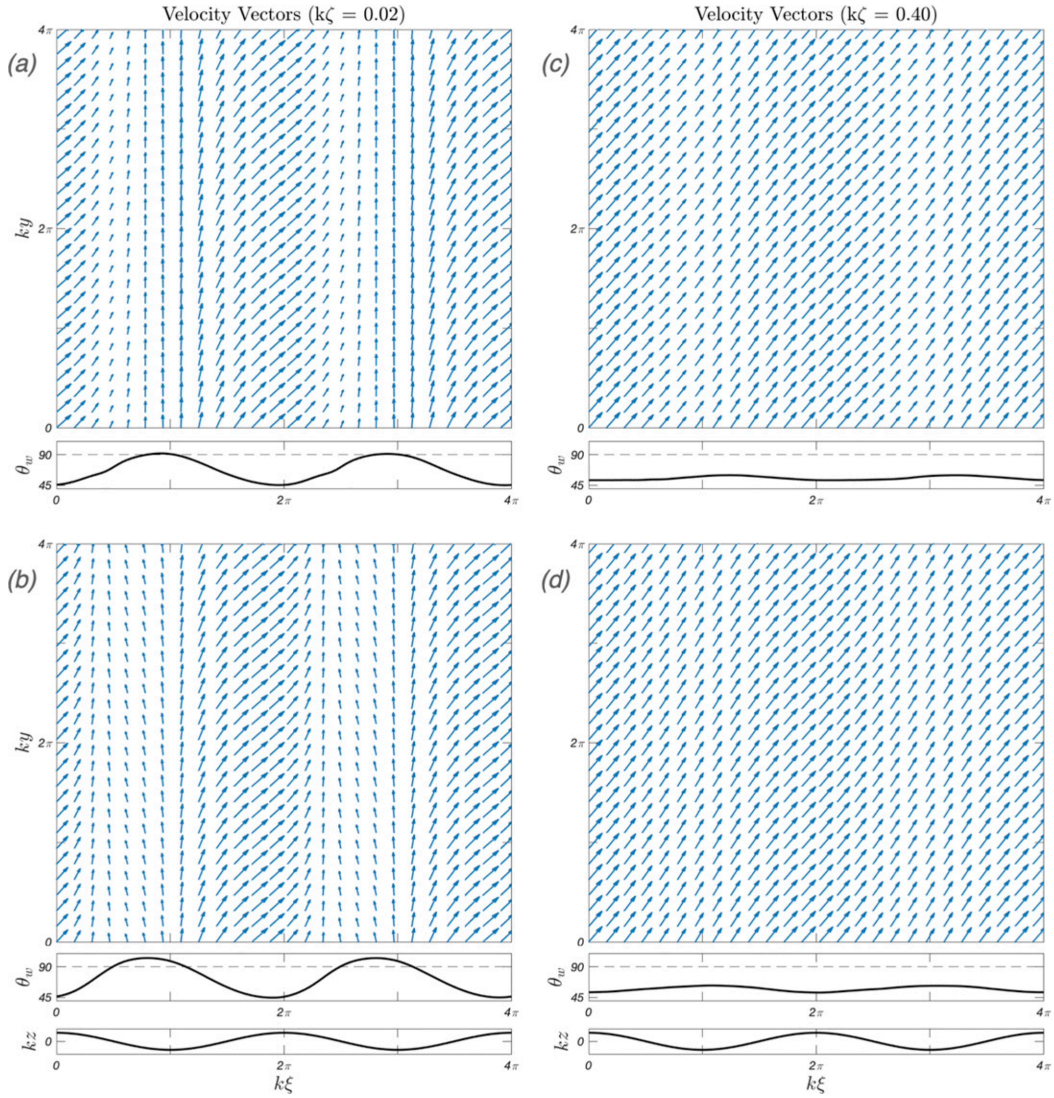

FIG. 10. Normalized phase-averaged velocity vector fields in the ξ–y coordinate (top) for waves following oblique wind and (bottom) for waves opposing oblique wind at (a),(b) $k\zeta = 0.02$ and (c),(d) $k\zeta = 0.40$. Mean wind angle θ_w is plotted below each vector field.

plotted (in the mapped ξ–y coordinate) of the phase-averaged velocity vectors $(\bar{u}, \bar{v})$ for mapped vertical levels $k\zeta = 0.02$ (directly above the surface) and $k\zeta = 0.40$ for waves following oblique wind (top row) and waves opposing oblique wind (bottom row). The mean wind angle $\theta_w = \tan^{-1}(\bar{v}/\bar{u})$ is plotted below each vector field. In both cases, the effect of the waves significantly modifies the velocity vectors close to the surface (Figs. 10a,b), which rapidly diminishes with height as shown by the almost uniform oblique velocity vectors at $k\zeta = 0.40$ (Figs. 10c,d). Near the surface, the vectors turn rapidly with the wave phase. Near the crest, the wind is strongest and relatively aligned with the oblique wind forcing direction. Just downstream of the crest where the flow separates, the wind becomes much weaker and turns rapidly to the left in the cross-wave direction. In opposing oblique wind, the vector even turns slightly upwind in the trough. From the trough to the following crest, the flow accelerates in the cross-wave direction first, then turns more oblique. This large cross-wave velocity is responsible for the enhanced along-wave vorticity (Figs. 4I,J) as discussed earlier.

e. Energy budget and turbulence closure parameterization

Next, we plot the energy budget inside the wave boundary layer (Fig. 11). As discussed in Part I, we use the derivation from Hara and Sullivan (2015) for the equations governing the wave-fluctuation energy, $E^w = (1/2)(\tilde{u}\tilde{u} + \tilde{v}\tilde{v} + \tilde{w}\tilde{w})$, and the turbulent kinetic energy, $\bar{e} = (1/2)(\overline{u'u'} + \overline{v'v'} + \overline{w'w'})$ in mapped coordinates. If the two equations are combined and normalized, the result yields:

Brought to you by University of Colorado Libraries | Unauthenticated | Downloaded 01/19/22 11:08 PM UTC

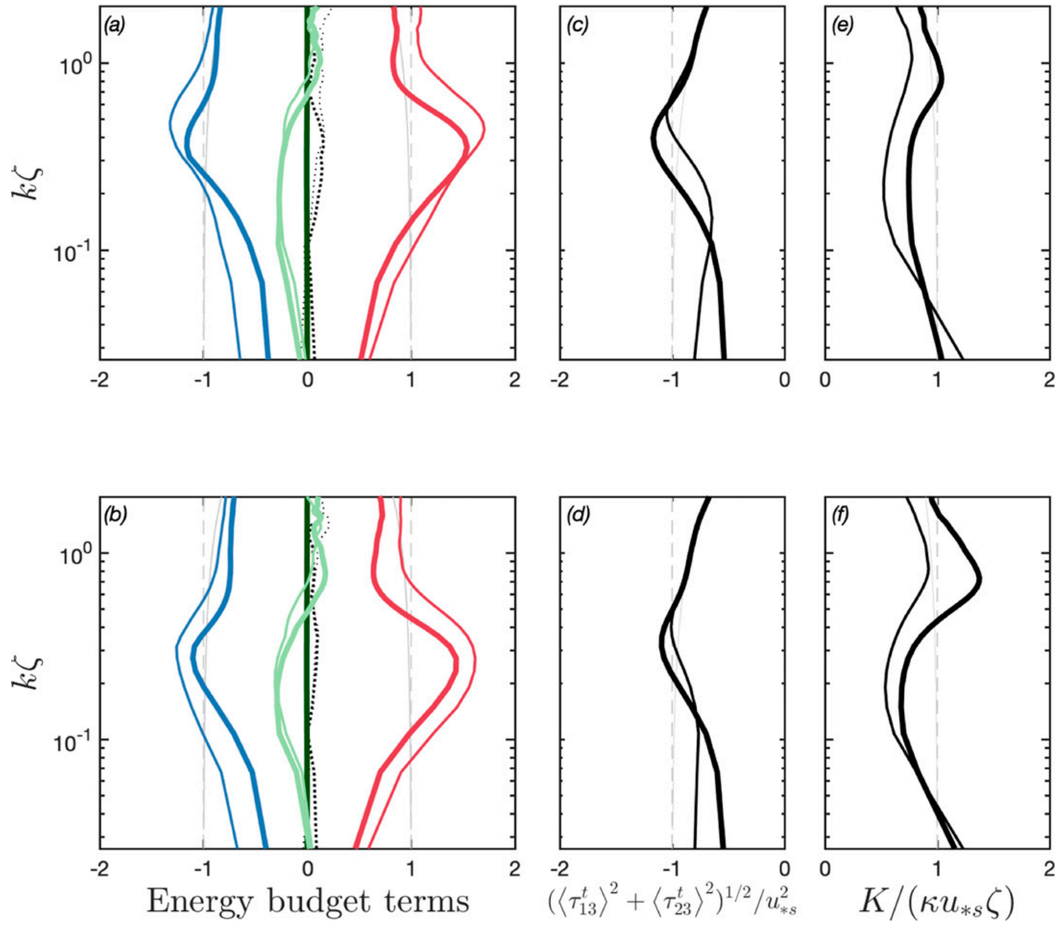

FIG. 11. (a),(b) Normalized vertical profiles of horizontally averaged energy budget terms. The first (pressure gradient), second (shear production), third (transport) and fourth (dissipation) terms of Eq. (3) are dark green, red, light green, and blue, respectively, with dotted black lines near zero equaling the sum of all energy budget terms. Thick (thin) lines are for aligned (oblique) wind. (c),(d) Normalized vertical profiles of horizontally averaged turbulent stress magnitude $\left[\left(\langle\tau_{13}^t\rangle^2 + \langle\tau_{23}^t\rangle^2\right)^{1/2}/u_{*s}^2\right]$. (e),(f) Normalized vertical profiles of eddy viscosity $[K/(\kappa u_{*s}\varsigma)]$.Waves (top) following and (bottom) opposing wind.

$$\left(\left\langle \tilde{u}\,\frac{1}{J}\right\rangle \frac{\partial P}{\partial x} + \left\langle \tilde{\upsilon}\,\frac{1}{J}\right\rangle \frac{\partial P}{\partial y}\right)\frac{\kappa\zeta}{u_{*s}^3} + \left(\langle\tau_{13}^{\rm tot}\rangle \frac{\partial\langle u\rangle}{\partial\zeta} + \langle\tau_{23}^{\rm tot}\rangle \frac{\partial\langle \upsilon\rangle}{\partial\zeta}\right)\frac{\kappa\zeta}{u_{*s}^3} - \frac{\partial(F^w + F^t)}{\partial\zeta}\,\frac{\kappa\zeta}{u_{*s}^3} - \left\langle\frac{1}{J}\,\epsilon\right\rangle\frac{\kappa\zeta}{u_{*s}^3} = 0, \tag{3}$$

where the second term is the shear production term (red lines), the third term is the transport term (light green lines; F^w and F^t are the vertical transport of E^w and $\bar{e}$, respectively), and the fourth term is the viscous dissipation term (blue lines). The first term arises because of the imposed pressure gradient (i.e., because the stress is not constant in the vertical) and is plotted in dark green, which is negligible. The sum of four energy budget terms is plotted as dotted black lines, and indicates that the energy budget is well satisfied. Thin gray lines represent the mean shear production (mean wind shear) over a flat wall for linearly decreasing stress (solid) and constant stress (dashed) with respect to $k\zeta$. Here, $(F^w + F^t)$ at the surface is equal to the energy flux into the waves. Refer to Hara and Sullivan (2015) for more details on the derivation of the energy budget in mapped coordinates.

In all cases the transport term is relatively small and the shear production is mostly balanced by the viscous dissipation at all heights. For waves both following and opposing wind, the shear production for waves in oblique wind (thin lines) is significantly enhanced compared to that for waves in aligned wind (thick lines) throughout the wave boundary layer. The viscous dissipation for oblique wind (thin blue lines) is also enhanced and balances the enhanced shear production. As discussed earlier, the enhanced wind shear magnitude throughout the wave boundary layer in the oblique wind cases is responsible for the increased far field wind speed and reduced equivalent roughness length (to the point of almost wiping out the wave effect) compared to those in the aligned wind cases. The energy budget analysis here suggests that the enhanced wind shear and the reduced equivalent roughness

Brought to you by University of Colorado Libraries | Unauthenticated | Downloaded 01/19/22 11:08 PM UTC

TABLE 1. List of run conditions and results of roughness enhancement z_o/z_{ob} and nondimensional wave growth/decay coefficient c_β for four LES simulations. The letters f and o in the run name represent waves following and opposing wind, respectively; the subscripts 22.5, 45, and 67.5 represent oblique wind runs at their respective angles. The values for $c_{\beta t}$, $c_{\beta n}$, and $c_{\beta p}$ refer to tangential turbulent stress, normal turbulent stress, and pressure contributions to c_β, and $c_{\beta\text{tot}}$ is the total.

Run	z_o/z_{ob}	$c_{\beta t}$	$c_{\beta n}$	$c_{\beta p}$	$c_{\beta\text{tot}}$
1.4f	4.60	2.7	1.6	13.2	17.5
$1.4f_{22.5}$	2.33	0.9	2.1	11.3	14.3
$1.4f_{45}$	0.90	0.6	3.2	6.4	10.2
$1.4f_{67.5}$	0.41	0.2	3.0	0.8	4.0
$1.4o_{67.5}$	0.46	−0.5	−2.1	−2.0	−4.6
$1.4o_{45}$	1.10	−0.9	−2.0	−6.9	−9.8
$1.4o_{22.5}$	3.40	−1.1	−1.1	−11.3	−13.6
1.4o	6.36	−3.5	−0.5	−13.0	−17.0

length with oblique winds are correlated with the enhanced viscous dissipation throughout the wave boundary layer.

As discussed in Part I, previous modeling studies have closed the turbulence in the wave boundary layer by parameterizing the TKE dissipation rate ($\langle\varepsilon/J\rangle$) using the turbulent stress ($\langle\tau^t\rangle$) (e.g., Makin and Kudryavtsev 1999; Hara and Belcher 2004). In Fig. 11, we compare the magnitude of turbulent stress (Figs. 11c,d) with the magnitude of viscous dissipation (blue lines in Figs. 11a,b). Their correlation is very strong in the aligned wind cases, but it is weaker in the oblique wind cases. In particular, if we compare the oblique cases (thin lines) with the aligned cases (thick lines), the turbulent stress is enhanced due to oblique wind only near the surface (roughly $k\zeta < 0.1$) and is slightly reduced further above, while the viscous dissipation is enhanced everywhere. Therefore, the turbulence closure based on ($\langle\tau^t\rangle$) would predict enhanced viscous dissipation near the surface and reduced dissipation above, that is, significantly underestimate the viscous dissipation integrated over the wave boundary layer. Then, it would underestimate the integrated mean wind shear and overestimate the resulting equivalent roughness length. This poses a challenge to existing modeling efforts of sea-state-dependent drag coefficient.

Since the turbulent stress and the mean vertical wind shear are well aligned as discussed earlier, it is possible to calculate the eddy viscosity K (magnitude of turbulent stress divided by magnitude of mean wind shear), shown in Figs. 11e and 11f. No apparent correlation is observed between K and the turbulent stress magnitude.

f. Wave growth/decay rate and equivalent roughness length

As in Part I, we calculate the energy transfer rate β from wind to waves using the surface stresses shown in Figs. 2A–D, and use the following common expression to compute the wave growth/decay rate coefficient c_β (positive/negative for growth/decay) for all conditions:

$$\beta = c_\beta \left(\frac{u_{*s}}{c}\right)^2 \frac{\rho_a}{\rho_w}\,\omega, \tag{4}$$

where ω is the wave frequency. The coefficient c_β is then evaluated based on the total energy flux ($c_{\beta\text{tot}}$), and including the contributions from the tangential turbulent stress only ($c_{\beta t}$), the normal turbulent stress only ($c_{\beta n}$), and the pressure only ($c_{\beta p}$). These quantities are summarized in Table 1. The results of $c_{\beta\text{tot}}$ and $c_{\beta p}$ are also plotted against $|\theta|$ in Fig. 12. Note that in some literature c_β is defined for the aligned wind-wave condition and the impact of misalignment θ between waves and wind stress is explicitly added. Here, our c_β includes the misalignment effect.

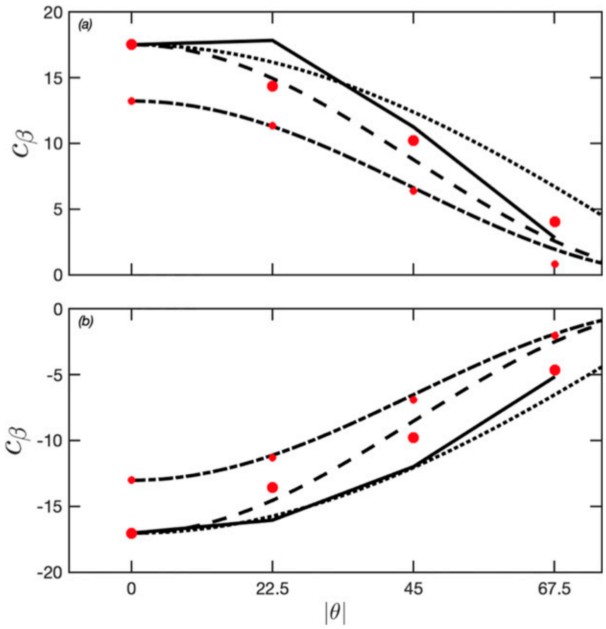

FIG. 12. Wave growth/decay coefficient c_β is plotted as a function of misalignment angle $|\theta|$ for waves following/opposing wind (top/bottom) for the current LES study (large red circles: $c_{\beta\text{tot}}$, small red circles: $c_{\beta p}$). Dot–dashed line shows $\cos^2(\theta)$ dependence of $c_{\beta p}$. Dashed, dotted, and solid lines show $\cos^2(\theta)$, $\cos(\theta)$, and $[U_{\lambda/2}\cos(\theta) - c]^2$ dependence of $c_{\beta\text{tot}}$, respectively.

The reduction of the pressure component only ($|c_{\beta p}|$, small red circles in Fig. 12) due to the misalignment is very close to the common parameterization of $\cos^2(\theta)$ (dot–dash lines) for both waves following and opposing wind (except for $\theta = 67.5°$ with waves following wind, where $c_{\beta p}$ is slightly below the parameterization). This also means that the pressure form drag is reduced by about 50% at $\theta = 45°$. If all turbulent stress contributions are added, the reduction of the total wave growth/decay rate coefficient $|c_{\beta\text{tot}}|$ (large red circles) due to wind-wave misalignment does not follow the $\cos^2(\theta)$ parameterization (dashed line) as closely; it is slightly below the parameterization at $\theta = 22.5°$ but above the parameterization at $\theta = 45°$ and 67.5°. Nevertheless, the $\cos^2(\theta)$ parameterization appears superior to the $\cos(\theta)$ parameterization (dotted line) or the $(U_{\lambda/2}\cos\theta - c)^2$ dependence (solid line, Donelan et al. 2012; Reichl et al. 2014), since the latter two significantly overestimate $|c_{\beta\text{tot}}|$ in smaller θ range, where the wave effects are more significant. Notice that the $(U_{\lambda/2}\cos\theta - c)^2$ dependence predicts a slight increase of $c_{\beta\text{tot}}$ from $\theta = 0°$ to 22.5°. This is because our simulations are performed with a fixed wind stress magnitude, and the along-wave wind speed at a

Brought to you by University of Colorado Libraries | Unauthenticated | Downloaded 01/19/22 11:08 PM UTC

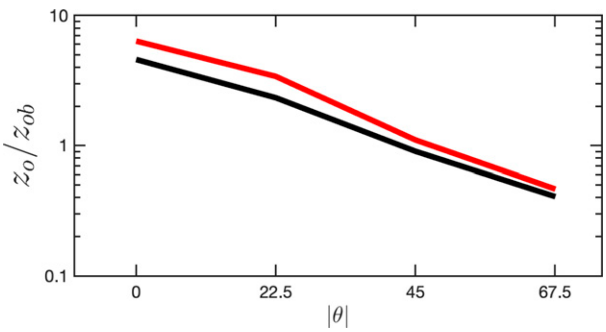

FIG. 13. Ratio of the equivalent surface roughness to the background (parameterized) surface roughness z_o/z_{ob} as a function of misalignment angle $|\theta|$ for waves following wind (black line) and waves opposing wind (red line).

height of half surface wavelength slightly increases as the wind stress direction increases, likely due to reduced wave impact.

As in Part I, we estimate the enhancement of the equivalent surface roughness z_o relative to the background roughness z_{ob} by comparing the wind speed magnitude at the top of the domain ($k\zeta = 2$) with and without waves. The results of the roughness enhancement z_o/z_{ob} are summarized in Table 1 and are plotted against $|\theta|$ in Fig. 13. As discussed earlier, the wave enhancement z_o/z_{ob} almost disappears at $|\theta| = 45°$. In fact, z_o/z_{ob} monotonically decreases with $|\theta|$ and becomes significantly less than 1 at $|\theta| = 67.5°$, that is, a wave train misaligned by 67.5° from wind can "reduce" the equivalent roughness length and the drag coefficient (compared to the flat surface case with the same background roughness length).

In summary, the wave form drag and the wave growth rate are both reduced due to misalignment θ between waves and wind stress, and the common parameterization of the angle dependence, $\cos^2(\theta)$, appears to be approximately valid. While the wave form drag remains significant (reduced by only about 1/2 at $\theta = 45°$), the wave impact on the equivalent roughness length almost disappears at $\theta = 45°$ and becomes negative (the equivalent roughness length and the drag coefficient are reduced) at larger misalignment angles. The latter finding is one of the most significant and surprising results of this study. This finding also suggests that existing models of sea-state-dependent drag coefficient may overestimate the impact of misaligned waves if the drag coefficient is simply assumed to increase with increasing wave form drag integrated over the entire wave spectrum.

4. Wind measurements from a moving platform

In the field, wind speed and stress measurements are often made on a moving platform that follows the up-and-down motions of the local swell. The wind stress is estimated by first subtracting the platform motion from the observed wind velocities, and then applying the eddy correlation method. Then the estimated wind stress is equivalent to $(\langle u'w' + \tilde{u}\tilde{w}\rangle, \langle v'w' + \tilde{v}\tilde{w}\rangle)$ in LES if the wave-following mapping does not decay with height. The 10-m wind speed is usually estimated from the observed mean wind speed, $(\langle u\rangle, \langle v\rangle)$ in LES, at the instrument height assuming the log wind profile. To simulate such wind speed and stress measurements, we modify the wave-following mapping to accommodate different degrees of vertical decay such that a decay coefficient σ is introduced to the vertical mapping given in Eq. (3) of Part I:

$$z = \zeta + a\cos(k\xi)e^{-\sigma k\zeta}. \tag{5}$$

All previous mapped results in this study have been shown with $\sigma = 1$, with the wave-following mapping gradually decaying to near Cartesian at the top of the domain. In this section, we use $\sigma = 0.0001$ such that the wave-following mapping barely decays with height, enabling a measurement of the wind velocities similar to what would be observed in the field on a wave-following platform, identical to the approach taken in Hara and Sullivan (2015).

In Figs. 14 and 15, we display the simulated moving platform measurements for wind speed, wind shear, and wind stress ($\langle u'w' + \tilde{u}\tilde{w}\rangle$) with $\sigma = 1$ mapping (solid lines) and $\sigma = 0.0001$ mapping (dashed lines). Figure 14 shows results for waves following and opposing waves as shown in Part I, and Fig. 15 shows results for the aligned and oblique wind results of Part II.

Overall, the results with $\sigma = 0.0001$ (dashed lines) are quite similar to those with $\sigma = 1$ (solid lines), as discussed by Hara and Sullivan (2015). Therefore, the results and discussions of the mean wind and wind shear profiles, presented in the previous sections and in Part I, remain valid, i.e., the wind profile can significantly deviate from the log profile and the wind direction can significantly vary in the wave boundary layer (say below $k\zeta = 1$).

Let us now focus on the wind stress measurements. The simulated measurement (Fig. 14i) indicates that for waves with low wave ages (slow waves, toward warmer colors) following wind, the wind stress magnitude is significantly underestimated below about $k\zeta = 0.5$ and almost approaches zero below $k\zeta = 0.1$, as pointed out by Hara and Sullivan (2015). As the wave age increases (toward blue) the stress magnitude is underestimated even at higher elevations, roughly up to $k\zeta = 1$. In the lower part of the wave boundary layer below $k\zeta = 0.2$–0.3, the stress magnitude gradually increases and becomes significantly overestimated near the surface at $c/u_{*s} = 11$. With the separation of the simulated wind stress into turbulent (Fig. 14e) and wave-coherent (Fig. 14g) components, it becomes clear that the magnitude of the turbulent component is consistently reduced in the wave boundary layer and that the main reason for the strong wave age dependence of the simulated stress is the pattern of the wave-coherent stress.

Although its occurrence is rare in the field, opposing steep swell can very strongly contaminate the wind stress measurements as shown in Fig. 14j. The stress magnitude is only slightly underestimated above $k\zeta = 0.4$ but it rapidly approaches zero near $k\zeta = 0.2$ and its direction becomes opposite (upward momentum flux) below, due to very strong wave-coherent stress (Fig. 14h).

Brought to you by University of Colorado Libraries | Unauthenticated | Downloaded 01/19/22 11:08 PM UTC

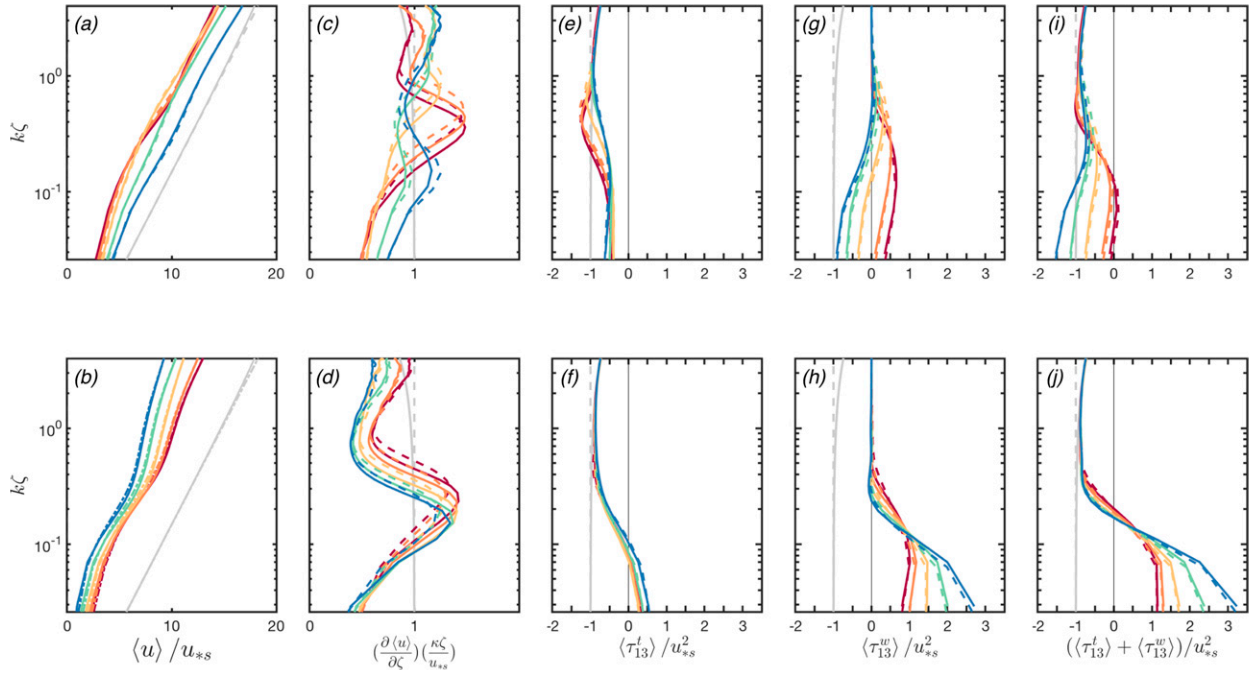

FIG. 14. Normalized wind speed, wind shear, and simulated wind stress measurement on a wave-following platform $[(\langle u'w' \rangle + \langle \tilde{u}\tilde{w} \rangle)/u_{*s}^2]$ for (top) waves following wind and (bottom) waves opposing wind for $|c/u_{*s}| = 1.4, 2.8, 5.6, 8.2$, and 11.0 (dark red, dark orange, light orange, light green, and blue). Normalized simulated wind stress is also plotted separately as the turbulent component $(\langle \tau_{13}^t \rangle / u_{*s}^2 = \langle u'w' \rangle / u_{*s}^2)$ and wave-fluctuation component $(\langle \tau_{13}^w \rangle / u_{*s}^2 = \langle \tilde{u}\tilde{w} \rangle / u_{*s}^2)$. Solid lines show results with vertical mapping using $\sigma = 1$ and dashed lines show results with $\sigma = 0.0001$. Gray lines show profiles for flat wall cases.

In Figs. 15c and 15f, the magnitude and angle of the simulated wind stress measurements for the results of Part II are shown ($\theta = 45°$ only). With waves following the oblique wind (thin orange dashed lines) the stress magnitude is underestimated and the stress angle significantly deviates from the correct angle ($-135°$) below $k\zeta = 0.5$. With waves opposing the oblique wind (thin blue dashed lines) the stress magnitude is also underestimated and the stress angle rotates by almost 290° from $k\zeta = 0.5$ to the surface. Note that motions of floating platforms are usually induced by long gravity waves with relatively large wave ages. Therefore, our results of oblique waves with wave age 1.4 is not readily applicable for such conditions.

In summary, the mean wind profile can significantly deviate from the log profile and the wind stress measurements can be strongly contaminated by the platform motion if the measurements are made below $k\zeta = 1$ of the dominant waves. For example, if the dominant wavelength is $\lambda = 50$ m, we would expect measurements to be contaminated below a height of about $\zeta = 8$ m above the sea surface.

5. Summary

In this study, we use large-eddy simulation to investigate turbulent airflow over steep strongly forced waves ($|c|/u_{*s} = 1.4$, $ak = 0.27$) following and opposing oblique wind (with wind stress direction misaligned from wave direction by $\theta = 22.5°, 45°, 67.5°$) as well as following and opposing aligned wind. Our results show that the phase averaged airflow in oblique wind maintains a signature of intermittent airflow separations characterized by enhanced vorticity originating along the windward face and detaching from the crest of the wave, resulting in reduced wind speed, TKE, vorticity, and dissipation in the leeward trough. These features in oblique wind cases appear to be as strong as those in aligned wind cases (Fig. 3).

These airflow features appear to modify the pressure fields and the resulting surface form drag due to oblique wind (Figs. 2k–n,A–D), resulting in wave growth/decay rate ($c_{\beta p}$, due to pressure stress alone) and the pressure form drag reduced from the aligned wind case, closely following the common $\cos^2(\theta)$ dependence. Even with the inclusion of the turbulent stress components the reduction of $c_{\beta \mathrm{tot}}$ seems to be reasonably close to the $\cos^2(\theta)$ dependence (except for very large θ values).

With waves following/opposing oblique wind ($\theta = 45°$), the mean wind speed (Figs. 7a,d,g,j) and the mean wind shear (Figs. 7b,e,h,k) are strongly modified. The directions of mean wind speed and mean wind shear significantly deviate from the direction of the wind stress $\theta = 45°$ (Figs. 7j,k). Most notably, we see a significant turning of the wind angles toward the surface ($\theta = 65°$–$68°$ for wind speed, $\theta = 63°$ for wind shear). Toward the top of the wave boundary layer the wind shear angle becomes close to $\theta = 45°$, but the wind angle remains significantly misaligned ($\theta = 52°$–$54°$). Although the direction

Brought to you by University of Colorado Libraries | Unauthenticated | Downloaded 01/19/22 11:08 PM UTC

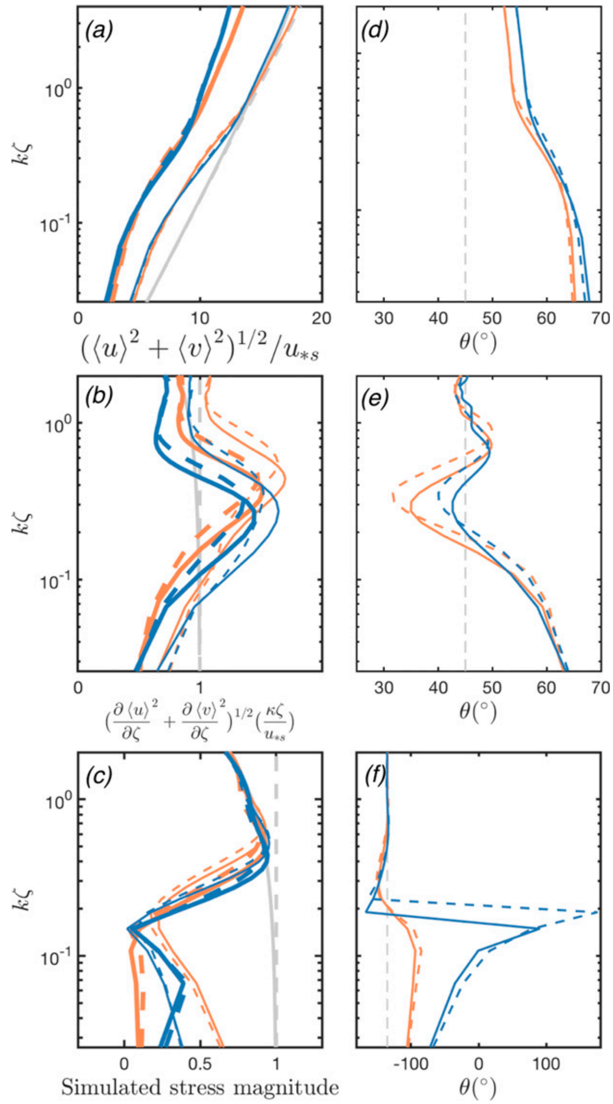

FIG. 15. Normalized magnitudes and angles of wind speed, wind shear, and simulated wave-following wind stress measurement $[(\langle\tau_{13}^t+\tau_{13}^w\rangle^2+\langle\tau_{23}^t+\tau_{23}^w\rangle^2)^{1/2}/u_{*s}^2]$ for waves following wind (orange lines) and waves opposing wind (blue lines) for aligned (thick lines) and oblique (thin lines) wind conditions. Solid lines show results with vertical mapping using $\sigma = 1$ and dashed lines show results with $\sigma = 0.0001$. Gray lines show profiles for flat wall cases.

of the mean wind shear varies with height in a complex manner, it is well correlated with the direction of the turbulent stress throughout the wave boundary layer; that is, the turbulent momentum flux remains mostly downgradient (Fig. 7k).

The momentum budget (partition of the total wind stress into turbulent, wave-coherent, and pressure stress components) in the along-wave direction (Figs. 8a,c) is quite similar in oblique and aligned wind cases, with enhanced positive wave-coherent stress (upward momentum flux) at midlevel due to airflow separations, pressure stress increasing toward the surface (downward momentum flux), and turbulent stress balancing the two. An analysis of the momentum budget in the cross-wave direction (Figs. 8b,d) highlights strong mid-level downward wave-coherent stress balanced by the reduced cross-wave turbulent stress. This feature appears related to the separating and reattaching flows (Figs. 9n,p,u,v), and is responsible for significant turning of the mean wind shear direction (Fig. 7k).

The most notable finding in this study is that waves oblique to wind appear to have little impact (at $\theta = 45°$) or negative impact (at $\theta = 67.5°$) on the equivalent roughness length and drag coefficient, even if such waves support significant wave form drag. We find that in oblique wind cases the wind shear magnitude is enhanced throughout the wave boundary layer (Fig. 7h), the far field wind speed is significantly increased (Fig. 7g), and the equivalent roughness length is reduced.

The energy budget analysis shows that the enhanced shear production (i.e., enhanced mean wind shear) is balanced by enhanced viscous dissipation throughout the wave boundary layer (Fig. 11) in the oblique wind cases. However, the turbulent stress in the wave boundary layer is not enhanced in a similar manner, which suggests that the existing turbulence closure schemes, relating the dissipation rate (or the mean wind shear) with the turbulent stress, may underestimate the mean wind shear and the far field wind speed and overestimate the equivalent roughness length and drag coefficient in the presence of misaligned waves.

In this study, we do not propose a new parameterization of the drag coefficient as a function of wind-wave misalignment. This is mainly because the total wind stress is expected to be dependent on integration of the wave form drag due to waves of all scales and directions, and a simple parameterization of the drag coefficient over complex seas, such as those with misaligned dominant waves, is not feasible. Instead, the aim of this study is to advance our understanding of how waves misaligned with wind interact with wind, and how the wave growth/decay rate, the mean wind profile, and the effective roughness are modified by such waves. The results from this study are expected to be beneficial for improving the sea-state-dependent drag coefficient parameterizations based on integration of wave form drag over complex seas.

This study focuses on wind over steep strongly forced misaligned waves, mainly because such waves support a bulk of the air–sea momentum flux, and therefore understanding the impact of such waves is critically important for improving the sea-state-dependent drag coefficient parameterizations. However, our choice of wave parameters is not likely applicable for conditions of dominant swell misaligned with wind, even under high wind tropical cyclone conditions. It is highly desirable to extend this study to include larger wave ages and reduced wave steepness in the future.

In this study, we have investigated the effect of oblique waves by maintaining the wind stress magnitude and altering its direction relative to the wave direction, because we think this is the most sensible approach to take as a first step. However, it is certainly of interest to expand the scope of study by comparing the aligned wave case with a different oblique wave case. One possibility would be to maintain the wind speed magnitude (at a certain elevation) and alter its direction. Another possibility

Brought to you by University of Colorado Libraries | Unauthenticated | Downloaded 01/19/22 11:08 PM UTC

would be to maintain the along-wave component of wind stress; that is, to compare the oblique (45°) case of wave age 1.4 and the aligned case of wave age $1.4 \times \sqrt{\sqrt{2}} = 1.66$ (given that the wave age is $|c|/u_{*s}$ and the wind stress is proportional to u_{*s}^2).

Finally, our LES results from both Part I and Part II suggest that wind speed and wind stress measurements performed on a wave-following platform can be strongly contaminated by the platform motion if the instrument is inside the wave boundary layer of dominant waves.

Acknowledgments. We acknowledge support of the National Science Foundation (Physical Oceanography) Grant OCE-1458984 (URI). We also acknowledge high-performance computing support from Yellowstone (ark:/85065/d7wd3xhc) and Cheyenne (doi:10.5065/D6RX99HX) provided by NCAR's Computational and Information Systems Laboratory, sponsored by the National Science Foundation.

Data availability statement. All large-eddy simulation data created and used during this study are openly available at http://dx.doi.org/10.17632/8vj68sr4rx.1.

REFERENCES

Ardhuin, F., T. H. C. Herbers, K. P. Watts, G. P. van Vledder, R. Jensen, and H. C. Graber, 2007: Swell and slanting-fetch effects on wind wave growth. *J. Phys. Oceanogr.*, **37**, 908–931, https://doi.org/10.1175/JPO3039.1.

Banner, M. L., 1990: The influence of wave breaking on the surface pressure distribution in wind–wave interactions. *J. Fluid Mech.*, **211**, 463–495, https://doi.org/10.1017/S0022112090001653.

Belcher, S. E., T. M. J. Newley, and J. C. R. Hunt, 1993: The drag on an undulating surface induced by the flow of a turbulent boundary layer. *J. Fluid Mech.*, **249**, 557–596, https://doi.org/10.1017/S0022112093001296.

Black, P. G., and Coauthors, 2007: Air–sea exchange in hurricanes: Synthesis of observations from the Coupled Boundary Layer Air–Sea Transfer experiment. *Bull. Amer. Meteor. Soc.*, **88**, 357–374, https://doi.org/10.1175/BAMS-88-3-357.

Bourassa, M. A., D. G. Vincent, and W. L. Wood, 1999: A flux parameterization including the effects of capillary waves and sea state. *J. Atmos. Sci.*, **56**, 1123–1139, https://doi.org/10.1175/1520-0469(1999)056<1123:AFPITE>2.0.CO;2.

Buckley, M. P., and F. Veron, 2016: Structure of the airflow above surface waves. *J. Phys. Oceanogr.*, **46**, 1377–1397, https://doi.org/10.1175/JPO-D-15-0135.1.

Burgers, G., and V. K. Makin, 1993: Boundary-layer model results for wind-sea growth. *J. Phys. Oceanogr.*, **23**, 372–385, https://doi.org/10.1175/1520-0485(1993)023<0372:BLMRFW>2.0.CO;2.

Cao, T., B.-Q. Deng, and L. Shen, 2020: A simulation-based mechanistic study of turbulent wind blowing over opposing water waves. *J. Fluid Mech.*, **901**, A27, https://doi.org/10.1017/jfm.2020.591.

Cronin, M. F., and Coauthors, 2019: Air-sea fluxes with a focus on heat and momentum. *Front. Mar. Sci.*, **6**, 430, https://doi.org/10.3389/fmars.2019.00430.

Donelan, M. A., 1999: Wind-induced growth and attenuation of laboratory waves. *Wind-Over-Wave Couplings: Perspectives and Prospects*, S. G. Sajjadi, N. H. Thomas, and J. C. R. Hunt, Eds., Clarendon Press, 183–194.

——, 2004: On the limiting aerodynamic roughness of the ocean in very strong winds. *Geophys. Res. Lett.*, **31**, L18306, https://doi.org/10.1029/2004GL019460.

——, and F. W. Dobson, 2001: The influence of swell on the drag. *Wind Stress Over the Ocean*, I. S. F. Jones and Y. Toba, Eds., 1st ed. Cambridge University Press, 181–189, https://doi.org/10.1017/CBO9780511552076.009.

——, ——, S. D. Smith, and R. J. Anderson, 1993: On the dependence of sea surface roughness on wave development. *J. Phys. Oceanogr.*, **23**, 2143–2149, https://doi.org/10.1175/1520-0485(1993)023<2143:OTDOSS>2.0.CO;2.

——, W. M. Drennan, and K. B. Katsaros, 1997: The air–sea momentum flux in conditions of wind sea and swell. *J. Phys. Oceanogr.*, **27**, 2087–2099, https://doi.org/10.1175/1520-0485(1997)027<2087:TASMFI>2.0.CO;2.

——, A. V. Babanin, I. R. Young, and M. L. Banner, 2006: Wave-follower field measurements of the wind-input spectral function. Part II: Parameterization of the wind input. *J. Phys. Oceanogr.*, **36**, 1672–1689, https://doi.org/10.1175/JPO2933.1.

——, M. Curcic, S. S. Chen, and A. K. Magnusson, 2012: Modeling waves and wind stress. *J. Geophys. Res.*, **117**, C00J23, https://doi.org/10.1029/2011JC007787.

Drennan, W. M., H. C. Graber, and M. A. Donelan, 1999: Evidence for the effects of swell and unsteady winds on marine wind stress. *J. Phys. Oceanogr.*, **29**, 1853–1864, https://doi.org/10.1175/1520-0485(1999)029<1853:EFTEOS>2.0.CO;2.

Edson, J. B., and Coauthors, 2007: The Coupled Boundary Layer and Air–Sea Transfer experiment in low winds. *Bull. Amer. Meteor. Soc.*, **88**, 341–356, https://doi.org/10.1175/BAMS-88-3-341.

——, and Coauthors, 2013: On the exchange of momentum over the open ocean. *J. Phys. Oceanogr.*, **43**, 1589–1610, https://doi.org/10.1175/JPO-D-12-0173.1.

Fan, Y., I. Ginis, T. Hara, C. W. Wright, and E. J. Walsh, 2009: Numerical simulations and observations of surface wave fields under an extreme tropical cyclone. *J. Phys. Oceanogr.*, **39**, 2097–2116, https://doi.org/10.1175/2009JPO4224.1.

Geernaert, G. L., 1988: Measurements of the angle between the wind vector and wind stress vector in the surface layer over the North Sea. *J. Geophys. Res.*, **93**, 8215, https://doi.org/10.1029/JC093iC07p08215.

——, F. Hansen, M. Courtney, and T. Herbers, 1993: Directional attributes of the ocean surface wind stress vector. *J. Geophys. Res.*, **98**, 16 571–16 582, https://doi.org/10.1029/93JC01439.

Grachev, A. A., C. W. Fairall, J. E. Hare, J. B. Edson, and S. D. Miller, 2003: Wind stress vector over ocean waves. *J. Phys. Oceanogr.*, **33**, 2408–2429, https://doi.org/10.1175/1520-0485(2003)033<2408:WSVOOW>2.0.CO;2.

Hara, T., and S. E. Belcher, 2002: Wind forcing in the equilibrium range of wind-wave spectra. *J. Fluid Mech.*, **470**, 223–245, https://doi.org/10.1017/S0022112002001945.

——, and ——, 2004: Wind profile and drag coefficient over mature ocean surface wave spectra. *J. Phys. Oceanogr.*, **34**, 2345–2358, https://doi.org/10.1175/JPO2633.1.

——, and P. Sullivan, 2015: Wave boundary layer turbulence over surface waves in a strongly forced condition. *J. Phys. Oceanogr.*, **45**, 868–883, https://doi.org/10.1175/JPO-D-14-0116.1.

Högström, U., E. Sahlée, A.-S. Smedman, A. Rutgersson, E. Nilsson, K. K. Kahma, and W. M. Drennan, 2015: Surface stress over the ocean in swell-dominated conditions during moderate winds. *J. Atmos. Sci.*, **72**, 4777–4795, https://doi.org/10.1175/JAS-D-15-0139.1.

Brought to you by University of Colorado Libraries | Unauthenticated | Downloaded 01/19/22 11:08 PM UTC

Holthuijsen, L. H., M. D. Powell, and J. D. Pietrzak, 2012: Wind and waves in extreme hurricanes. *J. Geophys. Res.*, **117**, C09003, https://doi.org/10.1029/2012JC007983.

Husain, N. T., T. Hara, M. P. Buckley, K. Yousefi, F. Veron, and P. P. Sullivan, 2019: Boundary layer turbulence over surface waves in a strongly forced condition: LES and observation. *J. Phys. Oceanogr.*, **49**, 1997–2015, https://doi.org/10.1175/JPO-D-19-0070.1.

——, ——, and P. P. Sullivan, 2021: Wind turbulence over misaligned surface waves and air–sea momentum flux. Part I: Waves following and opposing wind. *J. Phys. Oceanogr.*, **52**, 119–139, https://doi.org/10.1175/JPO-D-21-0043.1.

Kudryavtsev, V. N., and V. K. Makin, 2004: Impact of swell on the marine atmospheric boundary layer. *J. Phys. Oceanogr.*, **34**, 934–949, https://doi.org/10.1175/1520-0485(2004)034<0934:IOSOTM>2.0.CO;2.

Li, P. Y., D. Xu, and P. A. Taylor, 2000: Numerical modelling of turbulent airflow over water waves. *Bound.-Layer Meteor.*, **95**, 397–425, https://doi.org/10.1023/A:1002677312259.

Makin, V. K., and V. N. Kudryavtsev, 1999: Coupled sea surface-atmosphere model: 1. Wind over waves coupling. *J. Geophys. Res.*, **104**, 7613–7623, https://doi.org/10.1029/1999JC900006.

Mastenbroek, C., 1996: Wind-wave interaction. Ph.D. thesis, Delft Technical University, 119 pp., http://resolver.tudelft.nl/uuid:-b91093af-ccae-4d85-894e-af128cc9f59c.

Meirink, J. F., V. K. Makin, and V. N. Kudryavtsev, 2003: Note on the growth rate of water waves propagating at an arbitrary angle to the wind. *Bound.-Layer Meteor.*, **106**, 171–183, https://doi.org/10.1023/A:1020835211837.

Moon, I.-J., I. Ginis, T. Hara, H. L. Tolman, C. W. Wright, and E. J. Walsh, 2003: Numerical simulation of sea surface directional wave spectra under hurricane wind forcing. *J. Phys. Oceanogr.*, **33**, 1680–1706, https://doi.org/10.1175/2410.1.

——, T. Hara, I. Ginis, S. E. Belcher, and H. L. Tolman, 2004: Effect of surface waves on air–sea momentum exchange. Part I: Effect of mature and growing seas. *J. Atmos. Sci.*, **61**, 2321–2333, https://doi.org/10.1175/1520-0469(2004)061<2321:EOSWOA>2.0.CO;2.

——, J.-I. Kwon, J.-C. Lee, J.-S. Shim, S. K. Kang, I. S. Oh, and S. J. Kwon, 2009: Effect of the surface wind stress parameterization on the storm surge modeling. *Ocean Modell.*, **29**, 115–127, https://doi.org/10.1016/j.ocemod.2009.03.006.

Patton, E. G., P. P. Sullivan, B. Kosović, J. Dudhia, L. Mahrt, M. Žagar, and T. Marić, 2019: On the influence of swell propagation angle on surface drag. *J. Appl. Meteor. Climatol.*, **58**, 1039–1059, https://doi.org/10.1175/JAMC-D-18-0211.1.

Plant, W. J., 1982: A relationship between wind stress and wave slope. *J. Geophys. Res.*, **87**, 1961–1967, https://doi.org/10.1029/JC087iC03p01961.

Reichl, B. G., T. Hara, and I. Ginis, 2014: Sea state dependence of the wind stress over the ocean under hurricane winds. *J. Geophys. Res. Oceans*, **119**, 30–51, https://doi.org/10.1002/2013JC009289.

Snyder, R. L., F. W. Dobson, J. A. Elliott, and R. B. Long, 1981: Array measurements of atmospheric pressure fluctuations above surface gravity waves. *J. Fluid Mech.*, **102**, 1–59, https://doi.org/10.1017/S0022112081002528.

Sullivan, P. P., J. C. McWilliams, and E. G. Patton, 2014: Large-eddy simulation of marine atmospheric boundary layers above a spectrum of moving waves. *J. Atmos. Sci.*, **71**, 4001–4027, https://doi.org/10.1175/JAS-D-14-0095.1.

——, M. L. Banner, R. P. Morison, and W. L. Peirson, 2018: Turbulent flow over steep steady and unsteady waves under strong wind forcing. *J. Phys. Oceanogr.*, **48**, 3–27, https://doi.org/10.1175/JPO-D-17-0118.1.

Suzuki, N., Y. Toba, and S. Komori, 2010: Examination of drag coefficient with special reference to the windsea Reynolds number: Conditions with counter and mixed swell. *J. Oceanogr.*, **66**, 731–739, https://doi.org/10.1007/s10872-010-0060-6.

Tolman, H. L., and D. Chalikov, 1996: Source terms in a third-generation wind wave model. *J. Phys. Oceanogr.*, **26**, 2497–2518, https://doi.org/10.1175/1520-0485(1996)026<2497:STIATG>2.0.CO;2.

Walsh, E. J., and Coauthors, 2002: Hurricane directional wave spectrum spatial variation at landfall. *J. Phys. Oceanogr.*, **32**, 1667–1684, https://doi.org/10.1175/1520-0485(2002)032<1667:HDWSSV>2.0.CO;2.

Wright, C. W., and Coauthors, 2001: Hurricane directional wave spectrum spatial variation in the open ocean. *J. Phys. Oceanogr.*, **31**, 2472–2488, https://doi.org/10.1175/1520-0485(2001)031<2472:HDWSSV>2.0.CO;2.

Brought to you by University of Colorado Libraries | Unauthenticated | Downloaded 01/19/22 11:08 PM UTC